AD-A131 514 HOT ISOSTATIC PRESSING OF CERAMIC POWDER COMPACTS(U) 1/2
BATTELLE COLUMBUS LABS OH R R WILLS ET AL. 28 JUN 83
AFOSR-TR-83-0669 AFOSR-82-0238

UNCLASSIFIED F/G 11/2 NL

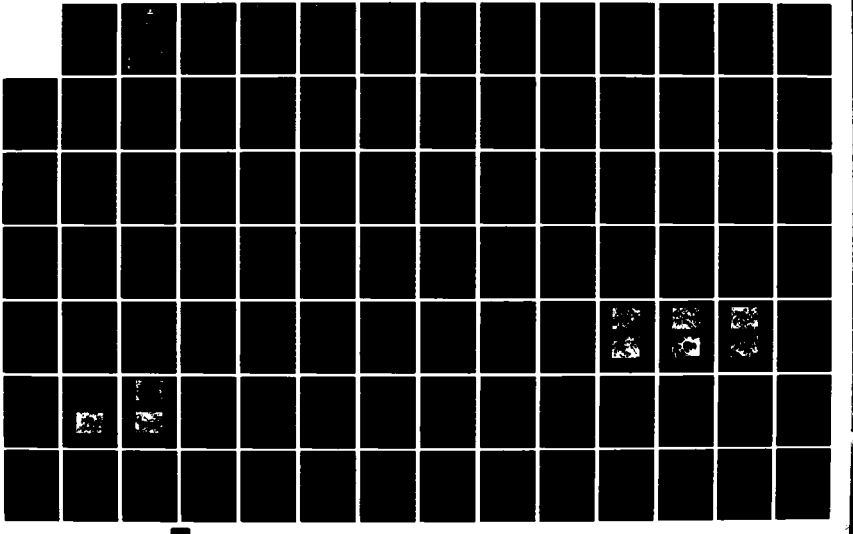

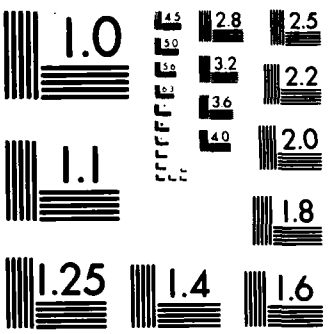

FIRST YEAR REPORT

on

HOT ISOSTATIC PRESSING OF CERAMIC POWDER COMPACTS

(AFOSR CONTRACT 82-0238)
(Project No. [redacted])
2306/A2

to

THE AIR FORCE OF SCIENTIFIC RESEARCH

June 28, 1983

by

R.R. Wills, J.K. McCoy, A.J. Markworth,
L.G. McCoy and L.E. Muttart

BATTELLE
Columbus Laboratories
505 King Avenue
Columbus, Ohio 43201

SECURITY CLASSIFICATION OF THIS PAGE (When Data Entered) UNCLASSIFIED

REPORT DOCUMENTATION PAGE

READ INSTRUCTIONS BEFORE COMPLETING FORM

1. REPORT NUMBER AFOSR-TR- 83-0669	2. GOVT ACCESSION NO. AD-A131 514
3. RECIPIENT'S CATALOG NUMBER	
4. TITLE (and Subtitle) Hot Isostatic Pressing of Ceramic Powder Compacts	5. TYPE OF REPORT & PERIOD COVERED Annual 1st year report 6/82-6/83
	6. PERFORMING ORG. REPORT NUMBER
7. AUTHOR(s) R.R. Wills, J.K. McCoy, A.J. Markworth, L.G. McCoy, and L.E. Muttart	8. CONTRACT OR GRANT NUMBER(s) AFOSR 82-0238
9. PERFORMING ORGANIZATION NAME AND ADDRESS Battelle Columbus Laboratories 505 King Avenue Columbus, Ohio 43201	10. PROGRAM ELEMENT, PROJECT, TASK AREA & WORK UNIT NUMBERS 6110 2F
11. CONTROLLING OFFICE NAME AND ADDRESS AFOSR/NE Bolling AFB, D.C. 20332	12. REPORT DATE June 28, 1983
	13. NUMBER OF PAGES 80
14. MONITORING AGENCY NAME & ADDRESS (if different from Controlling Office)	15. SECURITY CLASS. (of this report) UNCLASSIFIED
	15a. DECLASSIFICATION DOWNGRADING SCHEDULE

16. DISTRIBUTION STATEMENT (of this Report)

Approved for public release; distribution unlimited.

17. DISTRIBUTION STATEMENT (of the abstract entered in Block 20, if different from Report)

18. SUPPLEMENTARY NOTES

19. KEY WORDS (Continue on reverse side if necessary and identify by block number)

Hot Isostatic Pressing, Alumina, Mapping, HIP Densification Maps, Constitutive Equations

20. ABSTRACT (Continue on reverse side if necessary and identify by block number)

Several mechanisms contribute to the densification of ceramics during HIP. These can potentially be related to the kinetics of densification by the use of mechanism maps and a predictive methodology derived for determining parameter selection during HIP. The constitutive equations for final stage densification have been critically examined in terms of their underlying assumptions and the effects of changes in pore size, grain size, temperature, pressure, diffusion coefficient, density and the presence of residual gas

DD FORM 1 JAN 73 1473 EDITION OF 1 NOV 65 IS OBSOLETE

UNCLASSIFIED

SECURITY CLASSIFICATION OF THIS PAGE (When Data Entered)

pressure. A new algorithm for calculating and plotting mechanism maps has been derived. This algorithm reduces the number of data points needed to construct a complete map by a factor of 30.

Initial experiments performed at 1100°C and 102 MPa (15,000 psi) showed that a very small amount of grain growth occurred. Correlation of the experimental data with the theoretical predictions is quite good; if it is assumed that 1% residual porosity is a result of entrapped gases then excellent agreement between theory and experiment exists. Although the constitutive equations are supposed to be most applicable during the latter stages of densification, good agreement exists throughout the whole densification range.

TABLE OF CONTENTS

TABLE OF CONTENTS (Continued)

LIST OF TABLES

LIST OF FIGURES

TABLE OF CONTENTS (Continued)

Page

LIST OF FIGURES (Continued)

FIRST YEAR REPORT

on

HOT ISOSTATIC PRESSING OF CERAMIC POWDER COMPACTS (AFOSR CONTRACT 82-0238)

by

R.R. Wills, J.K. McCoy, A.J. Markworth,
L.G. McCoy and L.E. Muttart

June 28, 1983

INTRODUCTION

Hot Isostatic Pressing (HIP) was invented at Battelle's Columbus Laboratories by Saller, Paprocki, Dayton and Hodge [1]. The process involves the application of a highly pressurized gas at elevated temperatures to facilitate diffusion bonding, impregnation or the densification of metal or ceramic powders. Utilization of this process, to date, has largely been limited to metals, where unique properties have been derived from novel microstructural features induced by HIP processing of metal powders. This work suggested that the application of HIP processing to ceramic powder compacts will also result in unusual microstructural features and improved properties. Evidence for this hypothesis is given in the studies of Wills, et. al.[2] on the densification and high temperature mechanical properties of HIP'ed silicon nitride. These studies have shown that HIP enables full densification to occur in a system in which mass transport rates are sufficiently low to inhibit any measure of sintering. The creep rate of the ceramic is quite low, since the rate controlling step (dissolution at the grain-liquid interface) is identical to that in HIP'ing.

Several mechanisms contribute to densification during HIP. These vary with different types of ceramics and can be dependent upon the sintering stage as well as upon the applied temperature, pressure, and the particle size of the powder. The kinetics of densification during HIP can potentially best be related to the operative mechanisms by the use of mechanism maps[3].

Such maps have been used to describe fracture, deformation and sintering. Arzt, et. al.[4] recently termed such diagrams "HIP Maps" for the HIP process. Since there are several methods of HIP processing we propose to use the term "HIP Densification Maps" to describe the HIP pressure enhanced densification of ceramic powder compacts.

The first objective of this study is to derive a model to describe HIP densification using the concept of mapping to represent the data and mechanisms. The model is being tested by comparing experimental data with predicted values using alumina as the model material. Interpretation of the results is based upon the validity and limitations of assumptions used in the construction of the constitutive equations, the nature of the operative mechanisms and upon the accuracy of measurements.

A significant practical benefit will be obtained if good agreement between theory and practice can be demonstrated. Elimination of the "trial and error" approach to HIP parameter selection in favor of a predictive methodology will result in significant cost savings because of a reduction in the number of cycles needed to achieve desired results.

DEFORMATION MECHANISMS FOR ALUMINA

At a microscopic scale, densification of a powder by HIP may require the deformation of individual grains. Therefore, it is appropriate to consider the various mechanisms by which alumina deforms in order to derive constitutive equations for densification.

The following mechanisms have been treated in some detail in the literature: 1. slip, 2. dislocation creep, 3. diffusional creep, and, 4. interface-controlled creep. In the following sections, each of these mechanisms is discussed, along with applicable experimental data. A large fraction of the data discussed is from creep experiments performed on nominally fully-dense material rather than from experiments on densification of powders. While creep data alone are insufficient to predict densification rates, they are an important source of information. Figure 1, from Heuer, Tighe, and Cannon[5] shows deformation mechanisms for fully dense, MgO-doped alumina at 1500°C as a function of stress and grain size. This map is not quantitatively correct for pure Al_2O_3, but it does serve to illustrate the following discussion of deformation mechanisms.

Slip

At high temperature, alumina can deform by dislocation glide. The geometry of slip in alumina is summarized in Table 1. Slip occurs most easily on the basal plane, that is, on planes normal to the c axis. This system can be activated at temperatures as low as 900°C. Prismatic slip is more difficult; it requires higher stresses than basal slip and does not operate below 1150°C. As indicated in Table 1, the prismatic planes are parallel to the c axis. Pyramidal slip requires even higher stresses and temperatures. At macroscopic scales, pyramidal slip is not active below 1600°C.[6]

The existence of three different types of slip is peculiar to the hcp crystal structure. As indicated in Table 1, basal and prismatic slip provide only two independent slip systems each. According to the classical von Mises theory, however, five independent slip systems are required for general slip. As a result, plastic deformation of polycrystalline alumina requires at least one of the pyramidal slip systems. Under certain conditions, however, fewer slip systems are necessary.[7] A single crystal may be deformed in tension with only one slip system operating, and if grain boundaries are allowed to slide or open up, the number of slip systems necessary is reduced.

Measurements of stress and strain rate for alumina have been carried out by a number of investigators. Not surprisingly, the first type of slip studied was basal slip. Kronberg[8] measured stress at a variety of temperatures and strain rates. Analysis of his data suggests the following constitutive equations:

$$\dot{\varepsilon} = 5.7 \cdot 10^{9}\ s^{-1} \cdot \exp\left(-111\ \text{kcal} \cdot \text{mol}^{-1}/RT\right) \exp\left(\tau/(T \cdot 1.4\ \text{psi/K})\right) \qquad (1)$$

$$\dot{\varepsilon} = 1.42\ s^{-1} \exp\left(-89\ \text{kcal} \cdot \text{mol}^{-1}/RT\right) (\tau/55\ \text{psi})^{3.93} \qquad (2)$$

These both give a satisfactory fit to his data for the upper yield stress. In these equations, $\dot{\varepsilon}$ is the strain rate, T is the temperature, R is the gas constant, and τ is the applied shear stress. Kronberg's work revealed the presence of a pronounced yield-point effect; lower yield stresses were approximately hal[illegible] of the [illegible]er yield stresses.

Since Kronberg's work, several other measurements have been made of the yield point of alumina. Heuer, Tighe, and Cannon[5] have collected a number of results for both single crystals and polycrystals. Not included in this collection are the relatively recent measurements of Kotchick and Tressler[6] for slip in the prismatic system.

Dislocation Creep

Work by Cannon[9] on fully dense alumina indicates that creep at large grain sizes and high stresses is controlled by dislocation climb. In this regime, strain rate is proportional to σ^3 where σ is the applied stress. This is in agreement with Weertman's model for climb. Mohamed and Langdon[10] have fitted Cannon's data to this model, using the equation:

$$\varepsilon = A \left(\frac{Gb}{kT}\right) \left(\frac{\sigma}{G}\right)^n D_L^0 \qquad (3)$$

where A (=4) and n (=3) are dimensionless constants, G is the shear modulus, b is the Burgers vector, kT has its usual meaning, and D_L^0 is the diffusivity of oxygen in the lattice. Other investigators[5,11] appear to agree that oxygen diffusion controls dislocation climb. Because dislocation creep dominates only under rather unusual conditions, data on this mechanism are limited.

Diffusion and Diffusional Creep

Diffusion in ceramics is not as straightforward as diffusion in metals because of the requirement that the ceramic remain electrically neutral. Let us consider a simple case in which a fully dense ceramic is creeping by diffusion along grain boundaries and through the lattice. Both anions and cations may diffuse along both paths. Since anions may be diffusing primarily through the lattice at the same time that cations are diffusing primarily along the grain boundaries, the customary distinction between Coble and Nabarro-Herring creep is blurred. The effective diffusivity, D, for the combined processes is[10]:

$$D = \left(\frac{\alpha}{D_L^+ + 1.2\ (\delta/d) D_{GB}^+} + \frac{\beta}{D_L^- + 1.2\ (\delta/d) D_{GB}^-} \right)^{-1} \qquad (4)$$

This equation has been written to emphasize the analogy between diffusion of two types of ions along two paths and an electrical network with four conductances, two parallel pairs in series. The formula unit of the ceramic is assumed to be $A_\alpha B_\beta$. D_L^+ and D_L^- are the lattice diffusivities of cations and anions, respectively, D_{GB}^+ and D_{GB}^- are the grain boundary diffusivities, d is the grain diameter, δ is the effective width of the grain-boundary diffusion path, and the factor 1.2 δ/d corrects for the geometric differences between lattice and grain-boundary diffusion. For fully dense material, the strain rate that results from this combination of all four diffusion processes is

$$\varepsilon = 40\ \frac{\Omega\ \sigma\ D}{d^2 kT} \qquad (5)$$

This is the standard Nabarro-Herring creep equation except for the redefinition of the diffusivity. Modifications for densification are given below. Ω is the volume of the formula unit $A_\alpha B_\beta$, d is the grain size, and σ is the applied normal stress. The numerical value 40, as well as the value 1.2 in the previous equation, are approximate and are derived from assumptions concerning the geometry of the grains.

Perhaps the best collection of equations for diffusion coefficients for alumina has been compiled by Mohamed and Langdon[10], who drew heavily on the review of Cannon and Coble:[11]

	Reference	Equation
$\delta D_{GB}^{Al} = (8.6E\text{-}4 cm^3/s)\ \exp\ ((-419000\ J/mol\cdot K)/RT)$	10	(6)
$D_L^{Al} = (28\ cm^2/s)\ \exp\ ((-478000\ J/mol\cdot K)/RT)$	12	(7)
$\delta D_{GB}^{O} = (2.E\text{-}6\ cm^3/s)\ \exp((-226000\ J/mol\cdot K)/RT)$	10	(8)
$D_L^{O} = (1900\ cm^2/s)\ \exp\ ((-637000\ J/mol\cdot K)/RT)$	13	(9)

Diffusional creep occurs at moderate to low stresses and grain sizes, and various diffusion mechanisms can control the process, depending on experimental conditions. As shown in Figure 1, any one of the four diffusion mechanisms may control deformation.

Regardless of the relative sizes of the diffusion coefficients, diffusional creep predicts that strain rate will be proportional to stress. Experimental studies of creep in fine-grained alumina at low stresses frequently find that strain rate varies with a slightly higher power of stress, usually between 1 and 2. This non-viscous creep is presumably being measured in the range of transition to another creep mechanism, as described below.

Interface-Controlled Creep

An assumption in the derivation of the equation for diffusional creep is that grain-boundaries act as perfect sources and sinks of point defects and are free to slide.[14] At low stresses and small grain sizes, this assumption breaks down.

As Ashby[15] has suggested, one possibility is that the grain boundaries do not act as perfect sources or sinks of point defects. This would result in a threshold stress for deformation, so σ in Equation 5 would be replaced by $\sigma-\sigma_0$ where σ_0 is the threshold stress.

Another possibility is that the grain boundaries do not slide easily. If the boundaries are rough, any sliding must be accommodated by glide or climb of grain-boundary dislocations. Under this assumption, Burton[16] has obtained the constitutive equation

$$\varepsilon = M\,\delta^2/d \qquad (10)$$

where M is the mobility of grain-boundary dislocations and d is the grain size. Cannon, Rhodes, and Heuer[14] have pointed out that a threshold stress can be justified for this equation, too.

Interface control is potentially important in densification of fine-grained ceramics as well as in creep. A variety of explanations for interface control is found in the literature. The exact nature of this effect is still not clear.

CURRENT THEORY OF DENSIFICATION

In this section, the equations which are currently being used for modeling of densification are documented and explained. Descriptions of all variables used in this section are given in the Glossary, Table 2, along with values of constants and equation numbers for functions. Before considering the constitutive equations it is necessary to consider the treatment of pressure, shear modulus, and diffusion coefficients.

Pressure

In the previous discussion of creep, the tensile stress σ was assumed to be the driving force for deformation. To emphasize the hydrostatic nature of HIP, we use the net driving pressure P here. This quantity is simply the sum of the effects of the externally applied pressure, the internal pressure due to gases trapped in pores, and the surface tension of pores:[17]

$$P = \frac{P_e}{\rho} - P_i + \frac{4\gamma}{d_p} \tag{11}$$

The factor of $1/\rho$ multiplying the external pressure is intended as an approximate correction factor for the effect of porosity.

Shear Modulus

The data of Ryshkewitch[18] were fitted to the equation

$$G = 12.4\ \text{GPa}\ \sqrt[3]{1838-T} \tag{12}$$

for temperatures less than 1800 K where T is the temperature in kelvins. This appears to be in fair agreement with the more recent data of Soga and Anderson.[19]

Diffusion Coefficients

Values of diffusivities are listed below. These data have been given previously, but are repeated here for convenient reference.

$$\delta D_{GB}^{Al} = (8.6E\text{-}4 cm^3/s) \exp((-419000\ J/mol\cdot K)/RT) \quad (13)$$

$$D_L^{Al} = (28\ cm^2/s) \exp((-478000\ J/mol\cdot K)/RT) \quad (14)$$

$$\delta D_{GB}^{O} = (2.E\text{-}6\ cm^3/s) \exp((-226000\ J/mol\cdot K)/RT) \quad (15)$$

$$D_L^{C} = (1900\ cm^2/s) \exp((-637000\ J/mol\cdot K)/RT) \quad (16)$$

All of the necessary variables have now been described, either in the text above or in the Glossary. Let us now consider the constitutive equations for the various densification mechansism.

Densification by Lattice Diffusion

The following equation has been used to describe densification by lattice diffusion:

$$\dot{\rho} = \frac{12 D_L \Omega}{kT d^3 m} \frac{\sqrt[3]{1-\rho}}{1-\sqrt[3]{1-\rho}} P \quad (17)$$

Equation 17 comes from Wilkinson and Ashby,[20] modified for diffusion in ceramics. The necessary modification is the use of the volume of the formula unit ("molecular volume") Ω instead of the atomic volume and the inclusion of m, the number of atoms per formula unit for the species under consideration. The variable D_L is the lattice diffusivity for the appropriate species. The dependence on density is a result of Coble's model,[21] which assumes that vacancies diffuse from a spherical pore through a thick spherical shell before they reach a vacancy sink. The diameter of the shell is assumed to be equal to the grain size. This implies an assumption of one pore per grain, which is not necessarily realistic.

Densification by Grain-Boundary Diffusion

The equation for grain-boundary diffusion is also from Wilkinson and Ashby[20] with the same modifications as for Equation 17.

$$\dot{\rho} = \frac{36\delta D_{GB}\Omega}{kTd^3m} \quad \frac{1}{1-\sqrt[3]{1-\rho}} \quad P \qquad (18)$$

The variable D_{GB} is the grain-boundary diffusivity for the appropriate species. As in Equation 17, the dependence on density is the result of Coble's model. The assumption of a spherical grain with a pore at its center applies here just as for lattice diffusion, except that in this case it is assumed that three grain boundaries connect the pore with the surface of the spherical shell.

Equations 17 and 18 may seem to suggest that all diffusional densification mechanisms operate independently. If this were the case, the total densification rate due to diffusion would simply be the sum of the densification rates due to the diffusion of both species (Al and O) over both paths (lattice and grain boundaries). In fact, all four of these processes are coupled because of the requirement that the material remain electrically neutral. For creep, the correct description of this coupling is given by Equation 4. For densification, appropriate modifications must be made to take into account the fact that different density dependences arise in lattice and grain-boundary diffusion. For computational purposes, the faster diffusion path for the slower diffusing species is taken as rate controlling. The resulting densification rate is a good approximation to that which results from the coupling of all four mechanisms.

Densification by Diffusion, Alternate Treatment

Arzt, Ashby, and Easterling [4] have recently used a new expression for densification by grain-boundary and lattice diffusion combined. This expression is based on a more realistic geometry. Each grain is assumed to have the shape of a truncated octahedron. This shape is chosen because it is possible to fill space completely with such polyhedra. It is then assumed that pores are found at each vertex. Under these assumptions, the pore size is

$$d_p = d\left(\frac{1-\rho}{6}\right)^{1/3} \tag{19}$$

and the densification rate due to diffusion of a given species is

$$\dot{\rho} = 432\,\frac{\Omega(\delta D_{GB} + \frac{1}{2} d_p D_L)}{m\,kT\,d^3}\left[\frac{1-(1-\rho)^{2/3}}{3(1-\rho)^{2/3} - (1+(1-\rho)^{2/3})\ln(1-\rho) - 3}\right] \tag{20}$$

As in the standard treatment, diffusion of the various species is coupled by the requirement of electrical neutrality.

Densification by Dislocation Climb

The equation for densification by dislocation climb was derived by Wilkinson and Ashby.[22]

$$\dot{\rho} = \frac{3AD_L^0\,Gb}{2kTm}\,\frac{\rho(1-\rho)}{(1-(1-\rho)^{1/n})^n}\left(\frac{3P}{2nG}\right)^n \tag{21}$$

The geometry of the model used to derive this equation is similar to that assumed by Coble.[21] In this equation it is assumed that the driving pressure P is positive and that climb is controlled by diffusion of oxygen in the lattice.

The constitutive equations given above, along with the constants given in the Glossary, have been used to calculate the rate of densification. Most of our work was done using Equations 17 and 18 to describe diffusional densification and Equation 21 to describe dislocation densification. In a few cases, we have used Equations 19 and 20 in our work on diffusional densification because they are based on a more realistic geometry than are Equations 17 and 18. Unfortunately, Equations 19 and 20 were not available to us until very recently, and it was not feasible to rework all of the earlier calculations. Wherever Equations 19 and 20 are used in this report, their use is pointed out.

Our treatment of densification has considered only the final stage, that is, the stage in which pores may be treated as spherical and isolated. This limitation is of relatively minor importance. Our preliminary experimental data on aluminum oxide indicate that the initial stages of HIP

are generally quite fast compared to the final stage. As a result, the bulk of the HIP cycle is spent in final-stage densification. For completeness, it would be desirable to have descriptions of all densification stages, but from a practical viewpoint this is really not necessary since the final stage takes the largest fraction of the time.

There are two important limitations to the current theoretical treatment. The first is that grain growth is neglected, and the second is that we do not include the effect of gas pressurization of the pores. The exclusion of grain growth is very common; we are not aware of any paper which has included this effect. At the same time, the grain size is an extremely important factor in the constitutive equations. If grain-boundary diffusion controls densification, densification rate is proportional to the inverse cube of the grain size. In the coming year we will continue to critically evaluate our experimental data to determine what sort of grain-growth law is appropriate for HIP. The problem of grain growth is difficult in HIP for two reasons: 1. The pores tend to pin grain boundaries, resulting in a coupling between porosity and grain growth, and, 2. grain growth may leave some pores inside grains rather than on grain boundaries, and such pores can shrink only by lattice diffusion, not by grain boundary diffusion. Division of the pores into two classes may be necessary.

The effect of pressurization of pores is more straightforward than grain growth from a theoretical point of view. In principle, it has already been taken into account in Equation 11 for the driving pressure. From an experimental point of view, however, it is difficult to know in advance how much gas will be evolved from the powder upon heating. If the powder is thoroughly outgassed, this effect should normally be small.

COMPUTATIONAL METHODS

Over a decade has passed since Weertman and Weertman[3] introduced the concept of a creep map. During this time, the idea of mapping has gained wide acceptance. Maps have been calculated in two and three dimensions with many different sets of axes, and the idea has been applied to a great variety of materials and problems. In spite of this, no paper had been published which treated the problem of the method of calculating these maps. We have studied the problem, and our algorithm for calculating and plotting mechanism maps is presented in the paper[23] in the Appendix.

Not discussed in the paper, but still important in the construction of maps, is the question of interpolation schemes. This subject has also been neglected in the literature. In calculating a map, the rate of densification is calculated at a finite number of grid points. In general, contours or boundaries must be drawn which do not pass through the grid points, and it is necessary to interpolate between the values of the densification rate which were obtained at the grid points. The simplest way to do this is by bilinear interpolation: a nonlinear function f is approximated in the rectangular region $x_{min} < x < x_{max}$, $y_{min} < y < y_{max}$ by the function f* where

$$f^*(x,y) = a_0 + a_1(x-x_{min}) + a_2(y-y_{min}) + a_3(x-x_{min})(y-y_{min}) \qquad (22)$$

and the constants a_0, a_1, a_2, and a_3 are chosen so that

$$f^*(x_{min},y_{min}) = f(x_{min},y_{min}), \quad f^*(x_{max},y_{min}) = f(x_{max},y_{min}) \qquad (23)$$
$$f^*(x_{min},y_{max}) = f(x_{min},y_{max}), \quad f^*(x_{max},y_{max}) = f(x_{max},y_{max})$$

In less abstract terms, a bilinear function f* is used to approximate the function f over a given rectangular region, and f* is chosen in such a way that f and f* agree at the four corners of the region.

A bilinear interpolant is often a reasonable choice because of its simplicity. It is not a good choice for deformation mapping, however. Consider the function f defined by

$$f(x,y) = 1.1 \cdot 10^{x+3y} \qquad (24)$$

for all x and y. Figure 2 shows this function evaluted at all points x=0, 1, 2, 3 and y=0, 1, 2. Using these values and a bilinear interpolation scheme, f has been contoured at the level 10000. Note the poor agreement between the actual contour and the contour calculated by use of the bilinear interpolant.

Like the function discussed above, densification rates are highly nonlinear, and so bilinear interpolation performs poorly. The best solution to this problem is not to resort to a more complex interpolation scheme,

but to transform the function to make it more tractable. For example, if we define the function $g=\log_{10} f$, where f is the function in Equation 24 above, then

$$g(x,y) = \log_{10}(1.1) + x + 3y \qquad (25)$$

and it is immediately obvious that a bilinear approximant to g is exactly equal to g.

The effects of this with regard to densification mapping are illustrated in Figures 3 and 4. These two maps were calculated in exactly the same way, except that for Figure 3 interpolation was done on the densification rate itself and for Figure 4 interpolation was done on the logarithm of the densification rate. It is almost too obvious to point out that Figure 4 presents a far more pleasing appearance than Figure 3, even though both maps were calculated at the same grid density.

SENSITIVITY OF STUDIES

As an aid to evaluating the usefulness of the constitutive equations as a predictive tool, the effects of various factors on the densification rate have been studied using data for high purity alumina powder. This was accomplished by inserting appropriate values in the constitutive equations. Actual experimental work is described later.

Figures 5-11 are maps of densification rate as a function of temperature and applied pressure. Contours of constant densification rate are shown, labeled with $d\rho/dt$ where ρ is the fraction of theoretical density and t is the time in seconds. For all maps, the powder under consideration is pure alumina. The grain size, pore size and density vary from map to map and are specified in the captions. It is assumed that there is no internal pressurization of the pores due to trapped air or desorption of gases (such as water vapor) from the particle surfaces. For all maps except Figure 8, it is assumed that[20]

$$d_p = d(1-\rho)^{1/3} \qquad (26)$$

where ρ is the fractional density, d is the particle size, and d_p is the pore size. Equation 26 is equivalent to the assumption that there is one pore for each grain. It is not currently known how realistic this assumption is.

For various contours, the time necessary to achieve a 5% increase in density is as follows:

$d\rho/dt$	time
1.E-5	83 min
1.E-4	8.3 min
1.E-3	50 sec
1.E-2	5 sec

For all six maps, the constitutive equations predict that grain-boundary diffusion dominates over lattice diffusion for both aluminum and oxygen, and that aluminum diffusion is rate controlling. The maps were calculated using Equations 17 and 18. The effects of changing various parameters are summarized below:

Temperature and Pressure. Anny error in temperature of pressure will result in a corresponding shift of the map, either horizontally or vertically. The contours of constant densification rate have a rather steep slope, which indicates that temperature is more important than pressure in determining the densification rate. This is reasonable for diffusional densification: A major change in temperature can change the diffusivity by several orders of magnitude, producing a corresponding change in the densification rate. By contrast, a major change in the applied pressure is not likely to be larger than about one order of magnitude.

Density. The effect of a change in density can be seen by comparing Figures 5, 6, and 7. An increase in density results in a small decrease in the densification rate. The effect of density is complex. It enters Equation 18 both explicitly and implicitly. The implicit effect is through the density correction in Equation 11 for the driving pressure and through Equation 21 for the pore size, which also appears in Equation 11. Figures 5, 6, and 7 were all calculated by using Ashby's relationship (Equation 26) for grain size, density, and pore size. The calculated effect of density is small in the density range 80-95%. Not included in these calculations is

the effect of the internal pressure of air trapped in the pores, which will tend to cancel the effects of surface tension.

Pore Size. A decrease in pore size will generally increase the effective pressure on the compact; this results from the surface tension of the pores. This comparatively minor effect has been isolated in Figures 6 and 8, which differ only in pore size. The effects of surface tension enhance the driving pressure 1250 psi in Figure 6 and by 5800 psi in Figure 8. Except for a vertical displacement of the contours, the two maps are identical.

Grain Size. Grain size has a very strong effect on the rate of densification. The effect can be seen by comparing Figures 8 and 9. In the present case, the densification rate will be proportional to the inverse cube of grain size because the dominant mechanism of densification is grain-boundary diffusion. Even in the case of lattice diffusion, the densification rate is proportional to the reciprocal of the square of the grain size.

Aluminum Grain-Boundary Diffusivity. Since this process controls densification, any error in the value of the diffusivity used in this calculation will be reflected in a proportional change in the rate of densification. The effect of increasing the aluminum grain boundary diffusivity by a factor of ten can be seen by comparing Figures 6 and 11.

Other Diffusivities. Since the other diffusivities do not control densification, changes in these diffusivities will not affect the behavior of the material. A change of at least a factor of 30 in the ratio of the aluminum grain-boundary diffusivity to any other diffusivity would be necessary to make another dominant mechanism appear in the maps shown here.

As the preceding discussion makes clear, the densification rate can be profoundly changed by relatively modest changes in some of the parameters that describe the powder. In particular, differences of a factor of ten between the diffusion coefficient of two similar powders would not be surprising. This would strongly affect the predicted densification rate. Similarly, an error of a factor of three in the grain size would not be considered large, since it is often difficult to distinguish individual crystals from small hard agglomerates, but such an error in grain

size would change the predicted densification rate by almost a factor of 30 if grain-boundary diffusion is controlling. Therefore, it is not realistic to expect to predict HIP results a priori without allowing for these factors.

COMPARISON OF THEORETICAL PREDICTIONS WITH EXPERIMENTAL RESULTS IN THE LITERATURE

In this section, we compare theoretical predictions for the rate of densification during HIP with experimental results for densification during uniaxial hot-pressing. It is not unreasonable to suppose that the particles of powder are relatively free to move and slide during densification. If this is so, the macroscopic stress state of the powder compact should be approximately hydrostatic in both types of pressing, and experimental results should be quite similar. The comparisons were calculated using Equations 17 and 18.

Literature data on hot-pressing which can be compared to theory are surprisingly scarce. Some of the experimental papers treat doped powders, other present data in terms of densification rates (rather than density as a function of time) so that it will appear to support a given theory, and still other omit units on figures. Except as noted, the data discussed here are all for Linde A alumina, with a nominal particle size of 0.3 micron.

Some experimental results show a surprisingly large amount of variation from sample to sample. A good example of this is given by Fryer[24] who performed uniaxial hot-pressing on nine apparently identical samples. All samples were pressed at 1300°C and 5000 psi. The tabulated values for densification rate vary by a factor of more than 2.5. Viewed from a different perspective, the densities achieved after 1.5 hours of pressing varied from 89% to 96.3%. Similarly, Rossi and Fulrath[25-26] report densification rates which vary by almost a factor of 2 at 94% density. Rossi and Fulrath explained this variation as the result of water adsorbed on the powder. They calculated that 5% of a monolayer of adsorbed water will result in a terminal porosity of 5% after hot-pressing at 1250°C and 3000 psi. This explanation was supported by tests on outgassed powder. As a final example of variability from sample to sample, Sclosa, Dailly, and Hastings[27] produced hip-prosthesis heads from A16 alumina powder by hot-isostatic pressing. The porosity after two hours of HIPing at 140 MPa (20300 psi) and 1390°C varied between 0.3%

and 4%. In this case, the variability appears to result from peculiarities of the processing: the samples were first sintered without pressure to about 95% density, then HIPed without cans. The variation in final porosity may be the result either of the presence of surface-connected pores or of insufficient time to complete the densification.

Let us consider a few comparisons between theoretical predictions and experimental measurements of density as a function of time. Figure 12 shows data obtained at 1000°C by Felten.[28] The theoretical predictions using the nominal grain size for Linde A agree fortuitously well with the data. This is not expected, since Felten's data were taken at very low densities (30 to 55%) and the model is for final-stage densification. The low density suggests that non-diffusional mechanisms might be operating such as particle sliding or rearrangement, which are not included in our model.

Order-of-magnitude agreement is also seen at intermediate densities between theory and results obtained at 1200°C by Rossi and Fulrath.[25] The nominal particle size (0.3 μm) was again used in calculating the theoretical curves shown in Figures 13 and 14. Oddly, theory disagrees most strongly with experiment in final-stage densification, which is just where the theory should be at its best.

There are several possible reasons for disagreement between theory and experiment. First, the values of the diffusivities may be incorrect. The diffusivity of alumina is affected strongly by the presence of impurities such as MgO which produce extrinsic vacancies. Second, the grain size may be incorrect. A good deal of grain growth is expected in fine powders, and this will have a profound impact on the rate of densification. The assumption of a constant grain size seems to be universal in calculations of densification rate, but grain size is so important that a better treatment is necessary. A secondary effect of grain growth is that it can result in pores which are "stranded" away from grain boundaries. Shrinkage of such pores can occur only by lattice diffusion, not by grain-boundary diffusion. A hypothesis of stranded porosity is qualitatively consistent with the data of Rossi and Fulrath[26] and Rossi, Buch, and Fulrath.[25] Third, significant changes in the theoretical predictions can result from the choice of

geometrical descriptions for the pores and grains. The densification rate predicted by Equation 20 is typically twelve times that predicted by Equations 17 and 18, even though the only difference in the derivation of the equations is in the assumed arrangement of grains and pores.

It is difficult to make meaningful comparisons between theory and the literature, for the following reasons. First, experimental conditions were often poorly controlled, leading to poor reproducibility and difficulties in choosing the correct parameters for theory. Second, much of the literature data for hot-pressing were taken at densities which are so low that the theory is inappropriate.

POWDER CHARACTERIZATION

The material chosen for study is a high purity, calcined, dry ball-milled, α-alumina, (Reynolds RC-HP-DBM, Lot #BL-1004). The analyses performed to characterize the alumina powder are given in Table 3. Prior to distribution of the powder for the analyses, as-received material was riffled and reblended to ensure uniform sampling.

Spark Source Mass Spectroscopy

The results indicate that the powder contains a minimum of 99.986 weight percent alumina. The alumina sample was mixed with a high purity graphite (ultracarbon USP-1) to produce a conductive mixture for analysis. The results are reported in Table 4 as parts per million (ppm), weight basis. The highest impurities are Si (40 ppm), Mg (30 ppm), S (20 ppm), Na (15 ppm), Ga (10 ppm), Cl (3 ppm), F (< 3 ppm), Hg (< 3 ppm), and Cd (< 1.5 ppm). All other impurities are less than 1 ppm. Maximum total impurity level for the sample is 140.9 ppm or .014 weight percent.

Particle Size Analysis and Quantasorb BET Measurement

The results are summarized in Table 5 and Figures 15 and 16. Nitrogen with a He carrier gas was used as the adsorbate in BET measurements. The

sample was dried in an oven at 400°C for 24 hours prior to analysis. The specific surface area of the powder is 7.07 m^2g^{-1}. Mean equivalent spherical diameter (ESD) based on the specific surface area is 0.21 μm.

Particle size distributions were determined using a Particle Data, Inc. Elzone "/ADC-80XY" instrument. The instrument utilizes the same principals as the Coulter Counter to determine population and volume distributions. An alumina suspension was prepared by sonicating dried powder in distilled water containing sodium hexametaphosphate as a dispersant. Particle size distributions were determined from 0.55 μm to above 6.0 μm using a 24 μm aperture tube.

Figure 15 gives the population distribution for the powder. The distribution is normal but with a slight skew toward the finer particle size range. The size range of the distribution extends from 0.59 μm to 2.81 μm. The arithmetic mean of the distribution is 1.41 μm.

Figure 16 gives the volume distribution for the powder. The distribution is normal but slightly skewed toward the finer particle sizes. The size range of the volume distribution is continuous from 0.60 μm to 2.87 μm The isolated peaks above 2.87 μm occur because a large particle contributes significantly more than a small particle to total volume. The isolated volume peaks above 2.87 μm are probably due to only 1 to 10 large particles being counted in a particular channel out of a total of 50,000 particles counted during the measurement. Therefore, the isolated peaks are probably not statistically relevant. Furthermore, the isolated peaks are probably due to a few large agglomerates (see SEM results below) which did not disperse. Based on the continuous section of the distribution, the mean particle size of the volume distribution is 1.48 μm.

The presence and nature of agglomerates in the alumina powder are discussed in detail in the SEM and compaction curve sections. However, comparison of mean particle diameter from BET measurement (0.21 μm) and particle size analysis (1.41 μm) indicates significant numbers of agglomerates persisted in the suspension despite sonication and the dispersant present. The average agglomeration number from the ratio of mean particle volume to mean BET particle volume gives 303 primary particles in each agglomerate.

Compaction Curve

Results from the determinations of apparent density, tap density, and compaction ratio are given in Table 5. Pour density is 26.29 percent of theoretical density (TD) and tap density is 32.04 percent of TD. Compaction ratio is the ratio of the density of the powder pressed to 172.4 MPa (25 ksi) to the tap density. The compaction ratio for the alumina powder is equal to 1.36.

A sample of alumina powder was uniaxially pressed in a 12.7 mm steel die to determine relative density as a function of applied pressure. The compaction curve resulting from this procedure is given in Figure 17. The break in the curve between pressures of 0.7 MPa (101.5 psi) and 3.55 MPa (516 psi) indicates soft agglomerates are present in the powder. Whether significant breaks occur in the curve above 7 MPa indicating the presence of hard agglomerates is difficult to determine as plotted.

Donachie and Burr[29] showed that pressure as a function of relative void content resolves mechanisms involved in powder compaction. The compaction data are replotted as a Donachie-Burr plot in Figure 18. In Region I, particle restacking and rearrangement are taking place. The increased slope in Region II indicates soft agglomerate fracture is occurring. Evidence from the SEM micrographs discussed below indicates that hard agglomerates are present.

X-Ray Diffraction and Scanning Electron Microscopy Analysis

Alpha alumina was the only crystalline phase detected in the XRD analysis. Scanning electron photomicrographs of the powder are given in Figures 19, 20, and 21. The low magnification (30X) photomicrograph in Figure 19(a) indicates the as-received powder is composed of large, equiaxed agglomerates. Corners and edges of the roughly spherical agglomerates are rounded presumably due to self-milling. Scalp marks on some of the agglomerates indicate they are soft. This was verified

by lightly crushing with a glass slide as-received powder mounted on a SEM sample holder. A SEM photomicrograph of the crushed agglomerates at low magnification is given in Figure 19(b). As indicated in the figure, substantial quantities of the agglomerates were fractured by the light crushing.

Higher magnification views of as-received powder are given in Figure 20. The photomicrograph in Figure 20(a) shows the powder is composed of slightly ellipsoidal primary particles with diameters from 0.3 μm to 0.7 μm. However, there are regions in the photomicrograph showing from 2 to at least 20 particles in agglomerates. The photomicrograph in Figure 20(b) shows the surface and verifies the intimate contact between primary particle in the agglomerates. The primary particle surfaces are lobular.

To qualitatively determine whether the agglomerates in Figure 20 were hard or soft, an area of a crushed particle, indicated in Figure 19(b), was examined at higher magnifications. The views in Figure 21 at 10,000X and 30,000X for the area of the crushed particle show significant agglomeration despite the light crushing administered. This indicates that the agglomerates are hard.

SPECIMEN PREPARATION AND EVALUATION

Specimens were formed from as-received Reynolds RC-HP-DBM Al_2O_3 without added MgO, according to the following sequence:

- Vibration loaded in CIP bag
- Vacuum degas material in bag
- CIP at 50,000 psi
- Bisque fire at 1100 C for three hours
- Grind to 0.866 in diameter and 1.562 length
- Dry, then outgas at 1000°C under <1 μm Hg
- Load in 304 stainless steel cans and E-beam weld under vacuum.

These specimens were then HIP processed on a predetermined schedule consisting of the following steps; 1) pressurization at 15,000 psi, 2) heat to 1100°C at 400°C per hour, and, 3) HIP at 15,000 psi at 1100°C for zero, 15, 30, 60 and 180 minutes. In addition, one experiment was performed using a Battelle developed sensor to continuously monitor the shrinkage during HIP'ing. The initial and final dimensions are given in Table 6 together with the processing parameters. All specimens were examined using a scanning electron microscope to determine changes in particle and pore sizes, as well as particle morphology. Both polished and fracture surfaces were examined. Polished specimens were prepared with either alumina or diamond polishing media on standard metallurgical polishing wheels. Most polished specimens were etched in 10% phosphoric acid after optical examination and prior to SEM analysis. All specimens were ultrasonically cleaned in acetone and alcohol after polishing or etching.

Results of Measurements

The optical photomicrographs of the polished specimens (see Figures 22-26), show regions of varying porosity within each specimen. On examination of the photographs the observed changes with time may be explained as the effect of pore mobility from the regions of greater densification. As densification proceeds, coalescence of some pores is indicated, while other pores may be eliminated.

SEM photomicrographs of surfaces were taken at magnifications of 1000 to 25,000, but generally included magnifications of 5,000 and 10,000 for comparative evaluations. SEM views of fracture surfaces show sequential variation of surface topography. Specimen No. 11 is the only exception, showing more development of grains than expected.

There is an increase in angularity of particles, an increase in an average particle size from 0.2 μm to an average of 0.53 μm (0.3 to 0.8 μm range) and a decrease in pore count with longer processing times. Three photographs (see Figures 27-29) of the fracture surfaces of these specimens demonstrate this sequence of change. Figure 27 shows the surface of a

bisque fired specimen with an average particle size near .25 μm (range from 0.07 to 0.4 μm) and pore size average of less than 0.18 μm. The larger size "pores" in these specimens introduce an uncertainty in feature identification as pores vs. pull-outs. The pores are generally rectangular in shape and particles are generally spherical in shape. Figure 28 indicates that the average grain size after HIP'ing at 1100°C for 30 minutes is 0.382 μm (range from 0.2 μm to 0.5 μm). Average pore size is 0.2 μm (range from 0.1 to 0.4 μm). The pores are generally round or triangular in shape and particles show development of angularity, or flat contact faces. Figure 29 indicates an average grain size of 0.53 μm (range 0.3 to 0.8 μm) after HIP'ing at 1100°C for 3 hours. Pore sizes average about 0.1 μm and range from 0.5 μm to .2 μm. The pores are triangular in shape and particles show rather fully developed angularity. This data, which is summarized in Table 7, does indicate that a small amount of grain growth occurred during HIP'ing.

CONVERSION OF PROBE MEASUREMENTS TO DENSITIES

To correlate probe data with theoretical calculations or with direct measurements on the powder compact, it is necessary to use some sort of model for the geometry of the can and sample during densification. In this section we consider the corrections and conversions which must be made on the probe measurements to extract a value for the density.

One factor which must be considered in analysis of probe data is the effect of can wall thickening. Direct measurements showed that the thickness of the can body (sidewall) increased from 0.062" to 0.083" for can #7. To assume constant wall thickness would result in an error of 0.042", or roughly half of the measured change in diameter.

A second important factor is thermal expansion. Using the initial dimensions of the sample and thermal expansion data from the compilation of Touloukian,[30] the diameter of the sample is expected to increase by 0.012" upon heating from 20°C to 1100°C. This is a significant fraction of the measured change in diameter. In contrast, elastic compression of the sample is probably unimportant. The reduction in diameter due to 15000 psi external pressure is only about 0.0001".

We have assumed the following model for the geometry of the can. The alumina compact, or sample, is assumed to be a cylinder of constant mass but variable length, diameter, and density. The can body is a cylindrical tube of AISI 304 stainless steel with constant mass. The inside diameter of the tube is the same as the outside diameter of the alumina, and the length of the tube is the same as the length of the sample. A schematic drawing of the geometry is shown in Figure 30. The can body is assumed to be fully dense at all times.

The following discrepancies between the model and the actual geometry of the can and sample may be noted: 1. The ends of the sample do not remain flat during compaction but become slightly domed. 2. At the beginning of the experiment, there is a small gap between the sample and the can, both in diameter and in length. Since the stainless steel creeps before the alumina begins to densify, this gap disappears relatively early in the experiment. It is expected that these discrepancies will only have a small effect on the calculated densities.

During densification, dimensions were measured for the sample in can #7:

	Length	Diameter
initial	1.5625"	0.866"
final	1.3799"	0.750"

We have assumed that the following equation holds between the length and diameter of the sample:

$$\frac{L}{L^i} = \left(\frac{D_{sam}}{D^i_{sam}}\right)^{\alpha} \qquad (27)$$

where the variables are defined in Table 8. The assumption of Equation 27 is essentially arbitrary, and other relations such as

$$\frac{D_{sam}-D^i_{sam}}{D^f_{sam}-D^i_{sam}} = \frac{L-L^i}{L^f-L^i} \qquad (28)$$

might be suggested. However, the difference between Equations 27 and 28 is negligible; the diameters predicted by these two equations never differ by more than 0.00029".

Before treating the problem of converting probe readings to densities, let us predict the diameter of the can for a given temperature and density. For any density, the volume of the sample at 20°C is, by conservation of mass,

$$V_{20,sam} = V^{i}_{20,sam}(\rho^{i}/\rho) \tag{29}$$

while the volume of the can at 20°C is a constant since the steel does not densify. For both sample and can, the effect of temperature on volume is

$$V = V_{20}\ (1+\varepsilon)^3 \tag{30}$$

The following equations have been fitted to data[30] for the integrated thermal expansion

$$\varepsilon_{sam} = 7.2978E\text{-}6(T\text{-}293K)+7.8486E\text{-}10(T\text{-}293K)(T\text{-}800K) \tag{31}$$

and

$$\varepsilon_{can} = 1.7751E\text{-}5(T\text{-}293K)+5.0423E\text{-}9(T\text{-}293K)(T\text{-}800K) \tag{32}$$

These equations agree with the TPRC curves to within $\pm$0.015% over the temperature range 293 K < T < 1400 K.

Since the sample is cylindrical, the volume of the sample is

$$V_{sam} = \frac{\pi}{4} D^2_{sam}\ L \tag{33}$$

By combining Equations 27, 29, 30, and 33 one obtains

$$D_{sam} = \left(\frac{4V_{sam}\ D^{i\ \alpha}_{sam}}{\pi\ L^{i}}\right)^{\frac{1}{2+\alpha}} \tag{34}$$

while from Equation 46,

$$L = 4V_{sam}/\pi\ D^2_{sam} \tag{35}$$

Using Equations 29 to 35, it is possible to calculate the dimensions of the sample from the temperature and density plus known constants; α and the initial dimensions and density of the sample.

The can wall thickness may be obtained by solving the quadratic equation

$$V_{can} = \pi \, Lw(D_{sam} + w) \tag{36}$$

and the outside diameter of the can is given by

$$D_{can} = D_{sam} + 2w \tag{37}$$

We have therefore solved the problem of predicting the can diameter for any given density and temperature.

The problem of calculating density for a given temperature and probe reading requires a bit more computation. The can diameter is obtained by subtracting the probe reading from the known initial can diameter, and various densities are tested until one is found which predicts the same diameter as that obtained from the probe.

ANALYSIS OF EXPERIMENTAL DATA

In preparation for comparisons between experimental data and theoretical calculations, the geometrical model described in the previous section was used to convert probe readings into densities. Temperatures, pressures, and probe readings were tabulated from the original strip chart records. Linear interpolation was used between tabulated values. Since tabulation points were typically only a few minutes apart, more advanced interpolation schemes were unnecessary.

For each time at which data had been tabulated, the probe reading and temperature were used to calculate the fractional density. The effect of pressure was not included since it is negligible, as discussed above. The following additional data were also used in our calculations for can #7: 1. the measured initial and final dimensions of the sample, as given in the previous section, 2. the volume of the can, calculated by Equation from the measured final can wall thickness (0.083") and the final sample length, 3. the measured initial density of the sample, 0.658. The measured temperature and pressure profiles, along with the calculated densities, are shown in Figures 31 to 34. Also shown in these figures are immersion densities for samples in cans #7 and #9 to #12. These data provide a second experimental curve for the density as a function of time. The times at which the immersion densities are to be plotted are subject to an uncertainty of about 3 minutes since experimental conditions varied slightly from run to run. Theoretical rates of densification in Figures 31 to 34 were calculated with Equations 19 and 20, which apply to final-stage densification of a body composed of truncated octahedral grains with pores at the vertices.

Superimposed on the experimental data in Figure 31 are three curves of theoretically calculated densities for constant grain sizes of 0.25, 0.5, and 1.0 micron. The theoretical curves were calculated from the experimentally measured temperature and pressure. As in previous calculations, the effect of gas pressure in the pores was neglected.

Comparison of the theoretical and experimental curves in Figure 31 suggests the following observations:

1. The irregularities in the experimental curve are indicative of the amount of random error present in the calculated experimental densities. A likely source of random error is sticking of the probe rods. Systematic error is also present. This is made clear by the fact that the density trace for can #7 falls consistently below the immersion densities, including the immersion density for can #7. Sources of systematic error include errors in the measured dimensions of the sample and can, inaccurate values for the thermal expansion or the initial density of the alumina,

and incorrect assumptions regarding the can geometry. Systematic errors show up in the following ways: a) The initial density as calculated from the can geometry is .653 versus .658 for the directly measured density, b) The maximum calculated density is .973 versus .990 for the immersion density after decanning, c) As temperature drops at the end of the run, a density drop from .973 to .960 is calculated from the can geometry.

The most obvious explanation for the unexpected drop in the density is that the actual coefficient of thermal expansion is smaller that that which was used in calculating the density. Decreasing the coefficient of thermal expansion would reduce the slope of the curve for times greater than about 8.8 hours, where temperature is falling. However, such a change would also decrease the calculated density in the constant temperature region from 5.8 to 8.8 hours, resulting in poorer agreement with the immersion densities. In any case, a rather large change in the coefficient of thermal expansion is necessary. Even if the thermal expansion of the alumina is cut by 20%, there is still a density drop of 1.0% (from .969 to .959), which is only a minor improvement over the original drop of 1.3% (from .973 to .960).

2. A rather small but unmistakable increase in density is visible between 4.0 and 5.5 hours. It appears that the sample begins to densify at temperatures as low as 400°C. As the theoretical curves show, this is far too low a temperature for diffusional densification. The exact meaning of this apparent increase in density is not clear.

3. An abrupt increase in the densification rate is seen at about 5.5 hours. This feature, which is also seen in the theoretical curves, reflects the strong temperature dependence of the diffusivity.

4. The theoretical curves span a relatively small range of grain sizes, but show markedly different densification behavior. This shows again the great importance of grain size. Note that the curves for 0.25 and 0.5 micron grain sizes go rapidly to full density, but the curve for 1.0 micron grains only reaches a density of .924 after three hours at 1100°C.

5. The agreement between the experimental curve and the curve for 0.5 micron is remarkable. The equations used to derive the theoretical curve are intended for final-stage densification, but there is good agreement with the experimental rate of densification over a wide range of densities.

Since the final density of the alumina body was 0.99 and not 1.00, it is reasonable to assume that densification stopped due to gas pressure in the pores. Figure 32 is a recalculation of the results in Figure 31, except that it was assumed that the pores were filled with an ideal gas. The quantity of gas was set so that the gas pressure would exactly balance the combined external pressure and capillarity pressure at a density of 0.99. Expressed in terms of adsorbed water, 0.26 monolayer will result in 1% porosity at 15000 psi and 1100°C if the final grain size is 0.5 micron. This calculation assumes that the surface area of the bisque-fired body is the same as that of the original powder, 7.07 m^2/g.

At low densities, the effect of gas in the pores is small. As the final density is approached, however, the densification rate drops noticeably, and there is good agreement between the experimental curve and the theoretical curve for 0.5 micron. On the other hand, comparison with the immersion densities shows that the theoretical curve approaches final density too quickly.

A reasonable explanation for the slow approach to final density which is observed in the immersion densities is that there is grain growth. Rapid densification (5.5 to 5.8 hours) would take place while the grains are still small, with subsequent slower densification reflecting the increasing grain size. To test this hypothesis, we introduced a variable grain size into the densification model. The grain-growth law[31]

$$d^2 - d_o^2 = kt \tag{38}$$

was used, where d is the current grain size, d_o is the initial grain size, k is a variable parameter, and t is time. As a rough approximation, we assumed that no grain growth occurs below 1000°C and since the high temperature hold was almost isothermal, temperature dependence was ignored for temperatures over 1000°C. By fitting the measured grain sizes we obtained the grain growth equations

$$d = .3429\ \mu m \text{ for } t < 5.42 \text{ hour} \tag{39}$$

$$d = \sqrt{.1176\ \mu m^2 + .04959\ \mu m^2/h\ (t-5.42h)} \qquad (40)$$

for t >5.42 hour

Note that 5.42 hours is the time at which the temperature was 1000°C. The constant grain size in Equation 39 is chosen so that Equations 39 and 40 yield a continuous function.

Figures 33 and 34 contain the same experimental data as Figures 31 and 32, but the theoretical curves were calculated using a changing grain size defined by Equations 39 and 40 and for a range of diffusivities from the experimental value to 0.1 of this value. This simulates possible variations in the diffusivities. Figures 33 and 34 differ in that Figure 33 was calculated under the assumption that the pores were gas-free while for Figure 34 it was assumed that there was enough gas present to produce 1% porosity at a grain size of 0.53 micron. This grain size was chosen as it is the final grain size measured on material from can #7.

To compare theoretical results obtained with a changing grain size with those obtained with a fixed grain size, Figure 33 may be compared with Figure 31 and Figure 34 with Figure 32. The effects of grain growth are difficult to see. This is not surprising if one considers the rapidity of densification and the slowness of grain growth. For most of the theoretical curves, the final density is reached by 6.5 hours. At 6.5 hours, Equation 52 predicts that the grain size will have grown from .3429 micron to .4137 micron. This small amount of grain growth does not produce a marked change in the density curves.

TABLE 1. SLIP SYSTEMS FOR ALUMINA

Type	Slip System	Number of Independent Systems
Basal	$((0001))[[11\bar{2}0]]$	2
Prismatic	$((11\bar{2}0))[[1\bar{1}10]]$	2
Pyramidal	$((10\bar{1}1))[[01\bar{1}1]]$	5

TABLE 2. GLOSSARY

Symbol	Description	Value	Reference
A	Dimensionless Constant	4	10
b	Burgers Vector	4.75E-10m	10
d	Grain Size	(Variable)	
d_p	Pore Size	(See Eq. 19)	
D_{GB}^{Al}	Grain-Boundary Diffusivity of Al	(See Eq. 13)	10
D_L^{Al}	Lattice Diffusivity of Al	(See Eq. 14)	12
D_{GB}^{O}	Grain-Boundary Diffusivity of O	(See Eq. 15)	10
D_L^{O}	Lattice Diffusivity of O	(See Eq. 16)	13
G	Shear Modulus	(See Eq. 17)	
k	Boltzmann's Constant	1.3806E-23 J/K	
m	Number of Atoms of Diffusing Species in Formula Unit	(Variable)	
n	Dimensionless Constant	3	10
P	Driving Pressure	(See Eq. 11)	13
P_e	External Applied Pressure	(Variable)	
P_i	Internal Pore Pressure	0	
T	Temperature	(Variable)	
γ	Surface Tension	1 J/m^2	
δ	Effective Grain-Boundary Thickness	(See Eqs. 13,15)	
ρ	Fractional Density	(Variable)	
$\dot{\rho}$	Time Derivative of ρ	(See Eqs. 17,18,20,21)	
Ω	Volume of Formula Unit	4.20E-29m^3	10

TABLE 3. ANALYSES TO CHARACTERIZE ALUMINA POWDER

Analysis	Characteristic
Spark source mass spectroscopy (SSMS)	Trace element identification and amounts present
Particle size analysis (PSA)	Mean particle size and size distribution
Quantasorb BET measurement	Primary particle diameter and specific surface area
Compaction curve	Compaction behavior, tap density, apparent density, and the relative strength of agglomerates
X-ray diffraction (XRD)	Crystallographic phases
Scanning electron microscopy	Agglomerate and primary particle morphology

TABLE 4. MASS SPECTROGRAPHIC ANALYSIS OF REYNOLDS RC-HP-DBM ALUMINA WITHOUT MAGNESIA

Element	Impurity Level, ppmw	Element	Impurity Level, ppmw
Li	< 0.004	Co	< 0.06
Be	< 0.5	Ni	0.05
B	0.15	Cu	0.6
F	< 3	Zn	< 0.2
Na	15	Ga	10
Mg	30	Ge	< 0.1
Al	Major	As	< 0.02
Si	40	Se	< 0.5
P	0.04	Br	< 0.2
S	20	Rb	< 0.02
Cl	3	Sr	< 0.03
K	1.5	Y	< 0.04
Ca	0.5	Zr	< 0.2
Sc	< 0.04	Nb	< 0.05
Ti	< 0.03	Mo	< 0.05
V	< 0.01	Ru	< 0.2
Cr	0.01	Rh	< 0.06
Mn	0.04	Pd	< 0.3
Fe	5	Ag	< 0.2

TABLE 4. (Continued)

Element	Impurity Level, ppmw	Element	Impurity Level, ppmw
Cd	< 1.5	Er	< 0.15
In	< 0.03	Tm	< 0.05
Sn	< 0.15	Yb	< 0.15
Sb	< 0.1	Lu	< 0.05
Te	< 0.15	Hf	< 0.6
I	< 0.06	Ta	< 0.2
Cs	< 0.02	W	< 0.3
Ba	< 0.1	Re	< 0.2
La	< 0.05	Os	< 0.3
Ce	< 0.05	Ir	< 0.2
Pr	< 0.05	Pt	< 0.3
Nd	< 0.15	Au	< 0.1
Sm	< 0.15	Hg	< 3
Eu	< 0.07	Tl	< 0.2
Gd	< 0.15	Pb	< 0.4
Tb	< 0.05	Bi	< 0.07
Dy	< 0.15	Th	< 0.3
Ho	< 0.05	U	< 0.1

TABLE 5. SUMMARY OF CHARACTERIZATION DATA FOR REYNOLDS RC-HP-DBM ALUMINA WITHOUT MAGNESIA ADDITION

Mean Particle Diameter (BET), microns	0.21
Mean Particle Diameter (population), microns	1.41
Mean Particle Diameter (volume), microns	1.48
Average Agglomeration Number	303
Surface Area (BET) m^2g^{-1}	7.07
Pour Density, percent of theoretical	26.29
Tap Density, percent of theoretical	32.04
Compaction Ratio	1.36

TABLE 6. INITIAL AND FINAL SPECIMEN DIMENSIONS

Specimen Designation	#9	#11	#12	#10	#7(probe)
Initial can OD (in)	0.997	0.997	0.998	0.997	0.999
Initial can length (in)	2.025	2.012	2.006	2.022	2.084
End plug length (in)	0.437	0.437	0.437	0.437	0.499
Can wall thickness (in)	0.062	0.062	0.062	0.062	0.062
Sample Dia. (in)	0.866	0.866	0.866	0.866	0.866
Sample Length (in)	1.562	1.562	1.562	1.561	1.562
Can volume (cc)	26.072	25.986	25.735	26.031	---
Sample % Theoretical Density	65.05	65.18	65.68	65.78	65.80
Sample wgt (gms)	39.0331	39.1085	39.4110	39.4434	39.4666
Sample volume (cc)	15.0768	15.0768	15.0768	15.0671	15.0768
Final Can OD, (in)	0.9346	0.9247	0.9189	0.9154	0.9160
Can length (in)	1.8787	1.8512	1.8845	1.8412	1.8968
End plug thickness (in)	0.453	0.457	0.460	1.458	0.517
Can wall (in)	0.083	0.084	0.083	0.083	0.084
Sample dia (in)	0.7686	0.7575	0.7529	0.7494	0.7480
Sample length (in)	1.426	1.394	1.425	1.383	1.380
Can volume (cc)	19.505	20.197	20.600	20.675	NA
Final % theoretical density	87.53	94.64	96.81	97.74	98.99
Time at 1100 C, min	0	15	30	60	180
Time above 1000 C, min	15	25	45	74	213

OD = Outside Diameter

TABLE 7. GRAIN AND PORE SIZES

Specimen Designation	Time Above 1000 C Min.	Average (1) Particle/Grain Size (μm)	Average (1) Pore Size (μm)
Powder	None	.33	NA
B	Bisque only	.197	.194
9	15	.360	.309
11	25	.405	.19
12	45	.382	.20
10	74	.415	.15
7	213	.53	.10

(1) Determined from SEM photomicrographs.

TABLE 8. GLOSSARY OF PARAMETERS USED IN CAN SHRINKAGE CORRECTION FACTORS

D_{can}	Current Can Diameter
D_{sam}	Current Sample Diameter
D^{i}_{sam}	Initial Sample Diameter
D^{f}_{sam}	Final Sample Diameter
L	Current Length of Sample and can
L^{i}	Initial Length of Sample and can
L^{f}	Final Length of Sample and can
T	Temperature, kelvin
V_{can}	Current volume of sample
V_{sam}	Current volume of can
$V_{20,can}$	Volume of can at 20°C (constant)
$V^{i}_{20,sam}$	Initial volume of sample
w	Current can wall thickness
α	Dimensionless constant, $\ln(L^{f}/L^{i})/\ln(D_{sam}^{f}/D^{i}_{sam})$
ρ	Current Fractional density of sample
ρ^{i}	Initial Fractional density of sample

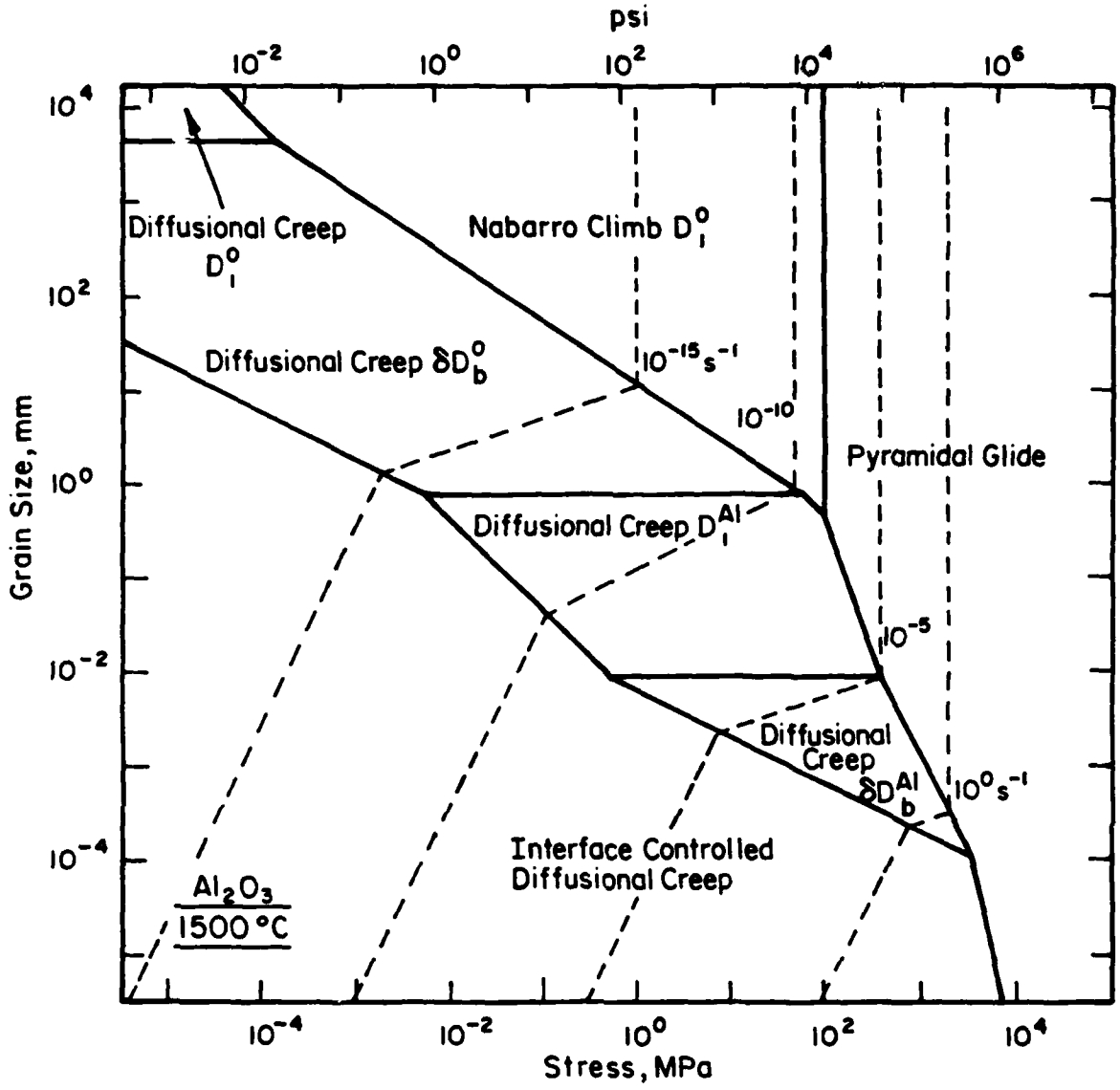

FIGURE 1. DEFORMATION MECHANISM MAP FOR MgO-DOPED Al_2O_3, SHOWING WIDE VARIETY OF DEFORMATION MECHANISMS AT 1500°C. DASHED LINES ARE CONTOURS CONSTANT STRAIN RATE. (AFTER HEUER, TIGHE, & CANNON 5)

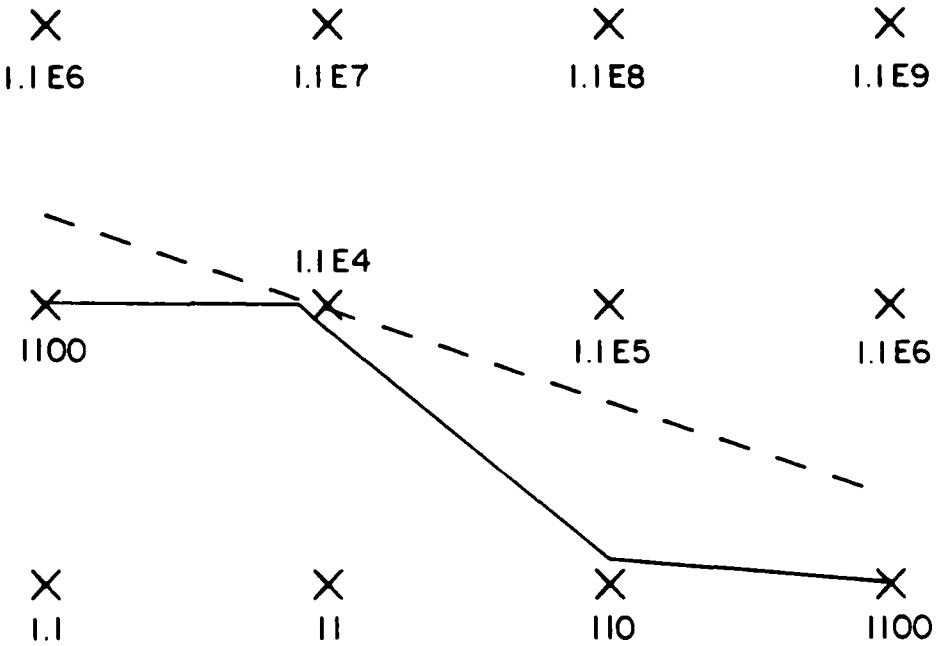

FIGURE 2. CONTOURING A NONLINEAR FUNCTION. A FUNCTION (See Eq. 12) IS EVALUATED AT GRID POINTS AND CONTOURED AT THE LEVEL 10000. DASHED LINE IS TRUE CONTOUR, SOLID LINE IS CONTOUR OBTAINED FROM BILINEAR INTERPOLANT.

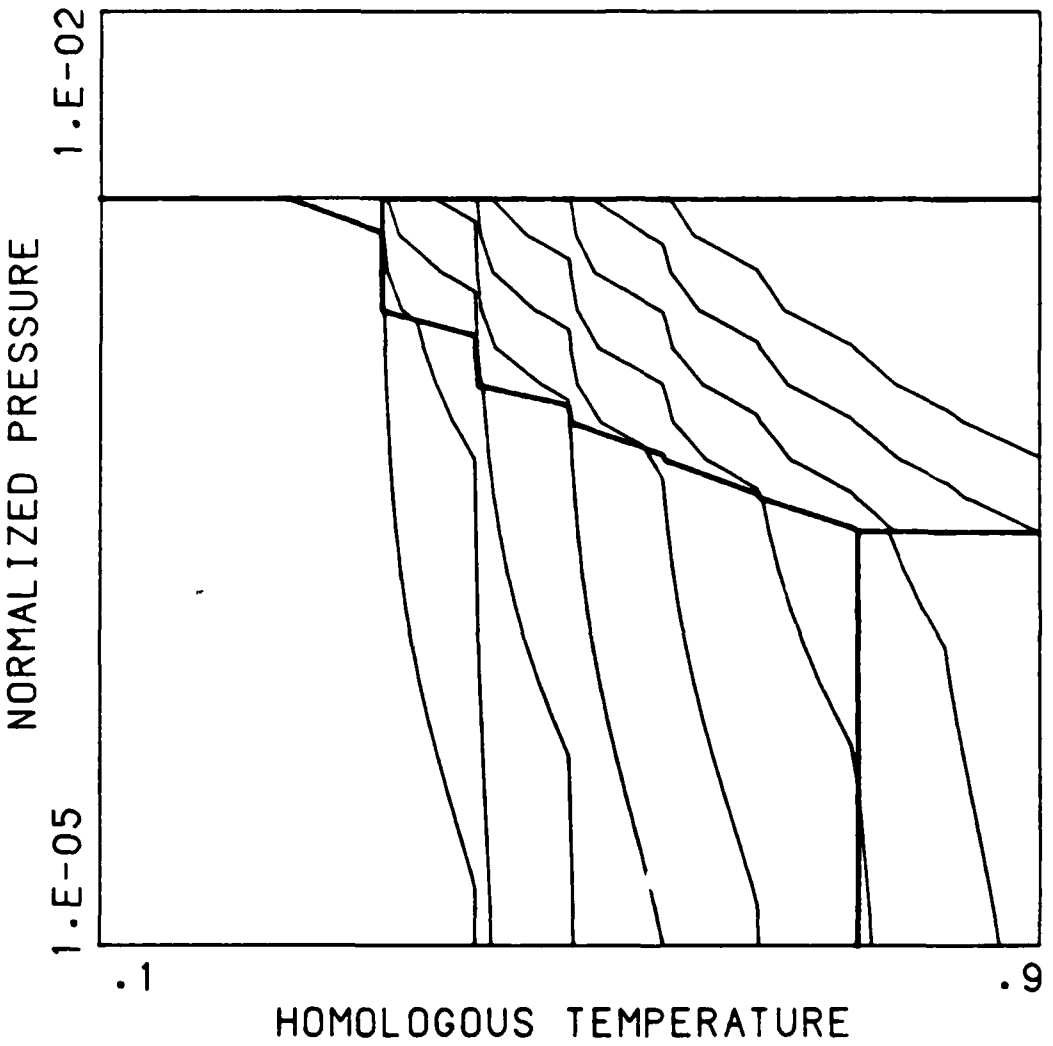

FIGURE 3. DENSIFICATION MAP CALCULATED BY USING A BILINEAR INTERPOLANT ON THE DENSIFICATION RATE.

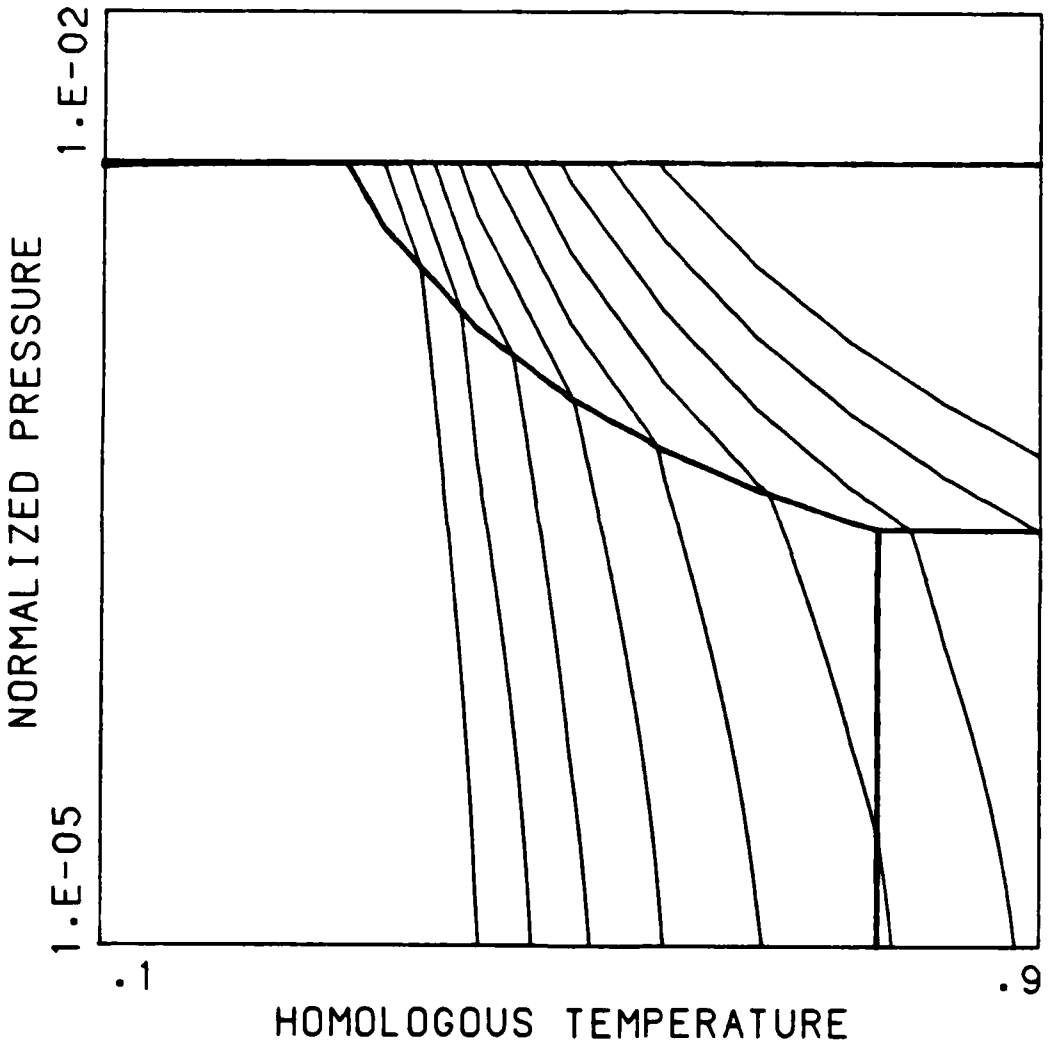

FIGURE 4. DENSIFICATION MAP CALCULATED USING A BILINEAR INTERPOLANT ON THE LOGARITHM OF THE DENSIFICATION RATE.

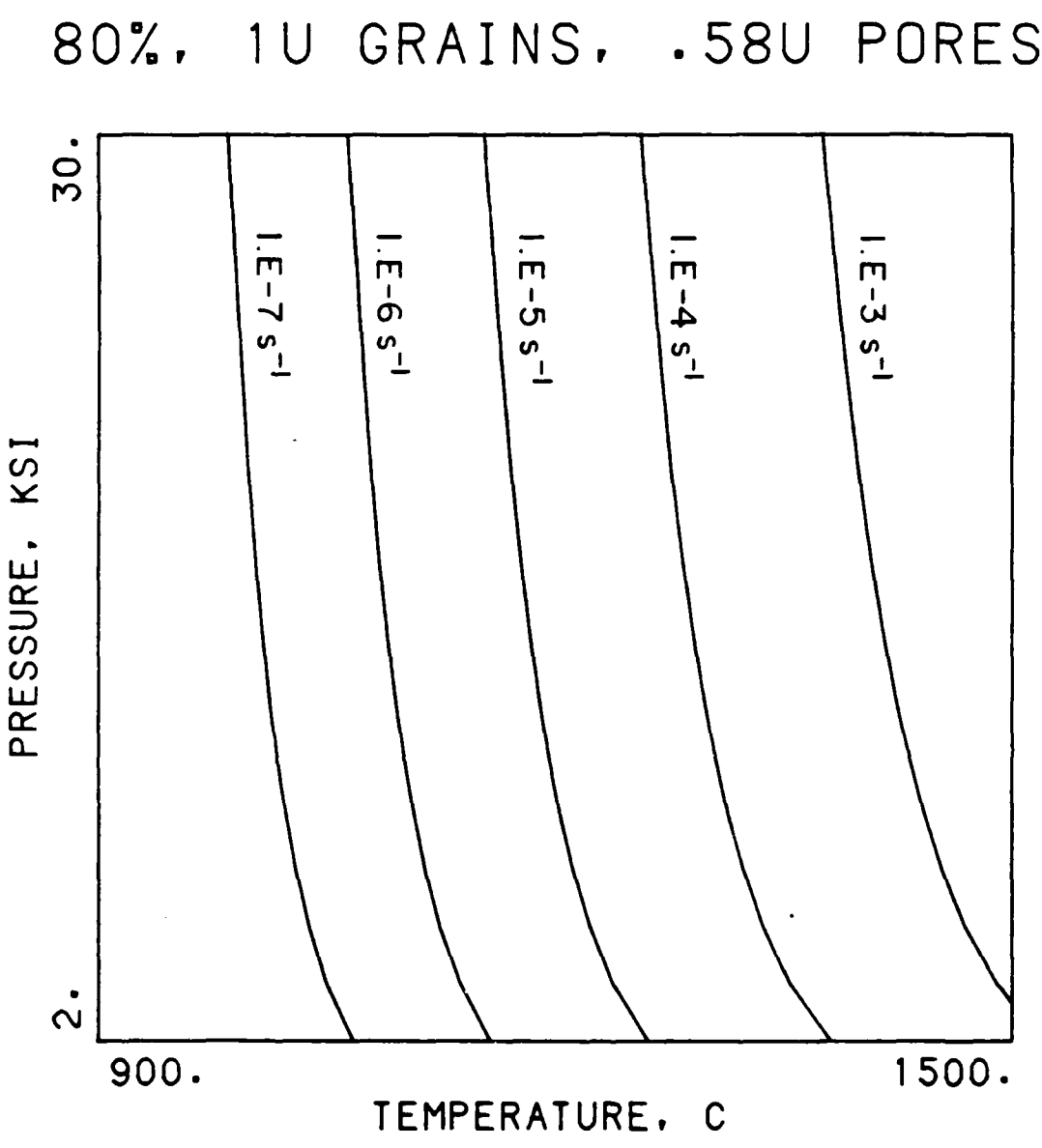

FIGURE 5. DENSIFICATION RATE FOR ALUMINA AT 80% DENSITY. GRAIN SIZE IS 1 μm, PORE SIZE IS 0.58 μm.

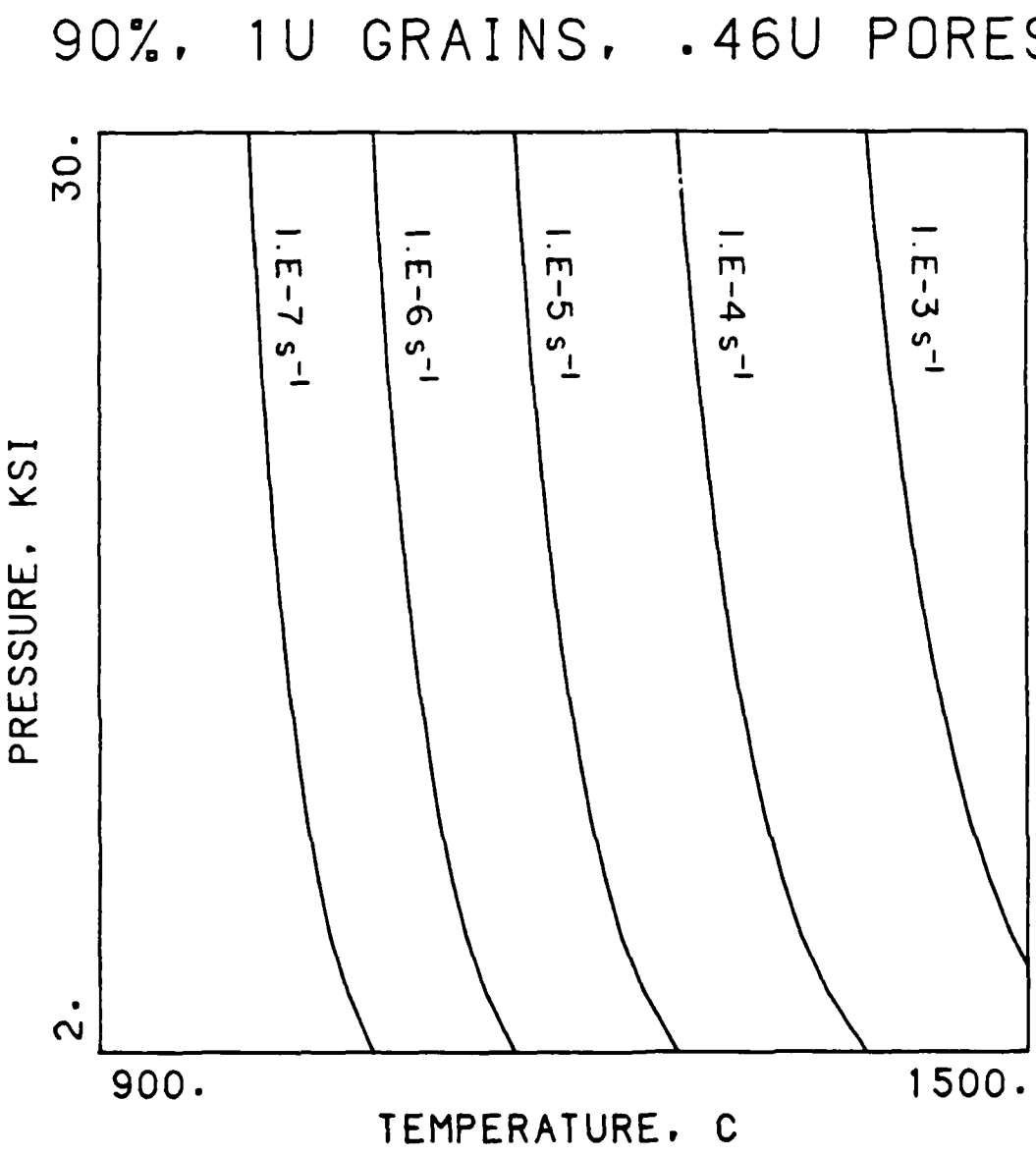

FIGURE 6. DENSIFICATION RATE FOR ALUMINA AT 90% DENSITY. GRAIN SIZE IS 1 μm, PORE SIZE is 0.46 μm.

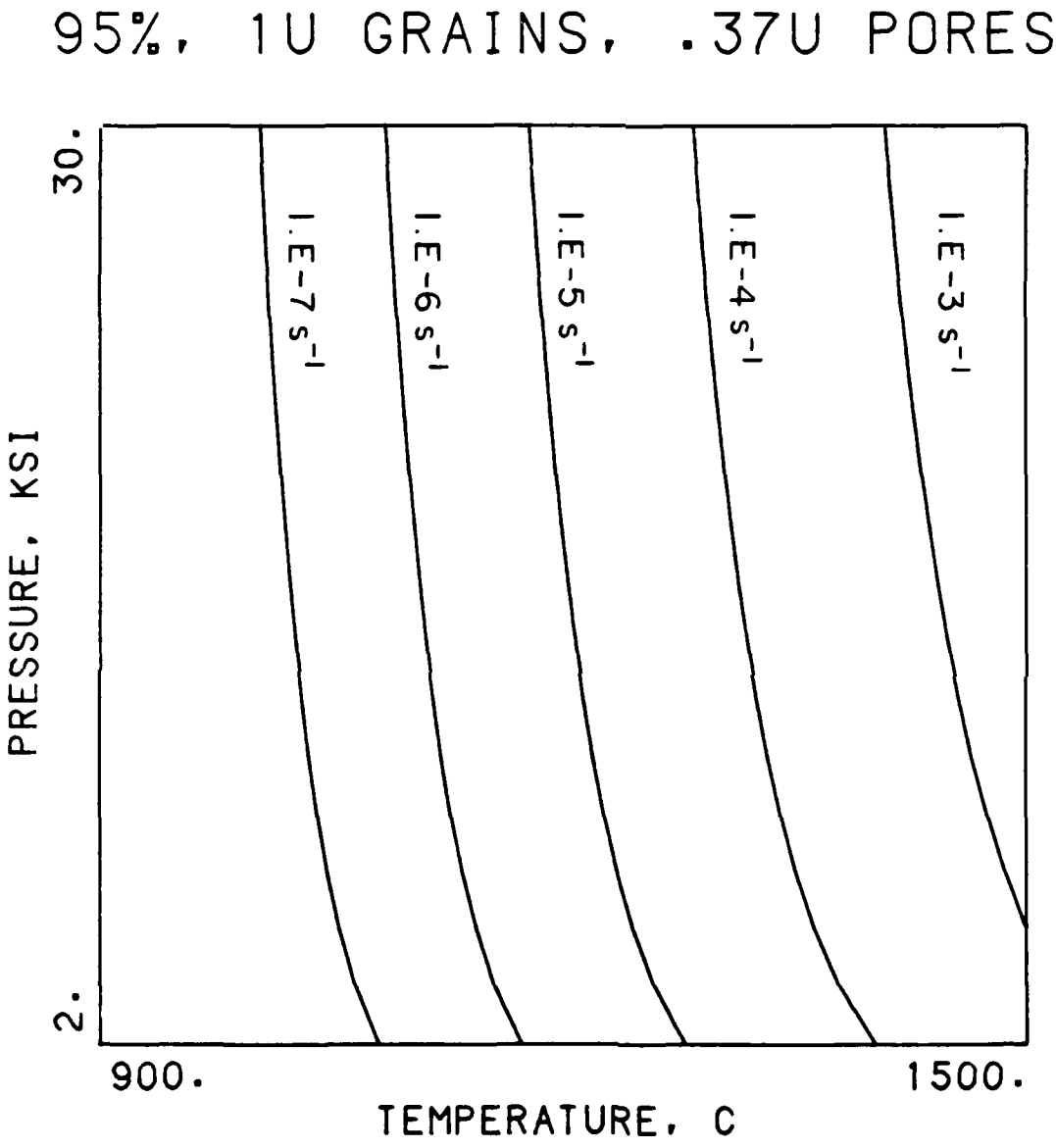

FIGURE 7. DENSIFICATION RATE FOR ALUMINA AT 95% DENSITY. GRAIN SIZE IS 1 μm, PORE SIZE IS 0.37 μm.

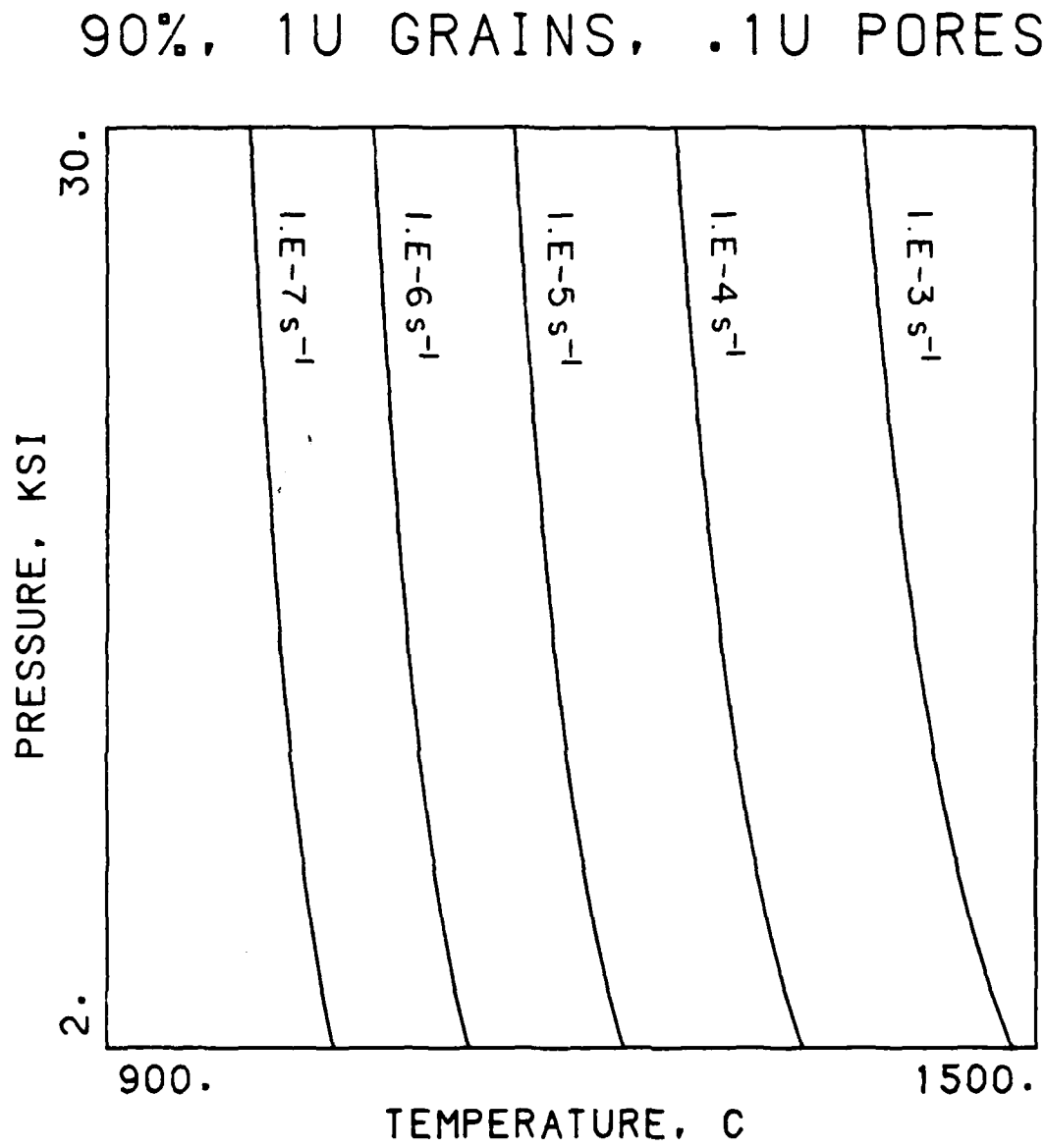

FIGURE 8. DENSIFICATION RATE FOR ALUMINA AT 90% DENSITY. GRAIN SIZE IS 1 μm, PORE SIZE IS 0.1 μm.

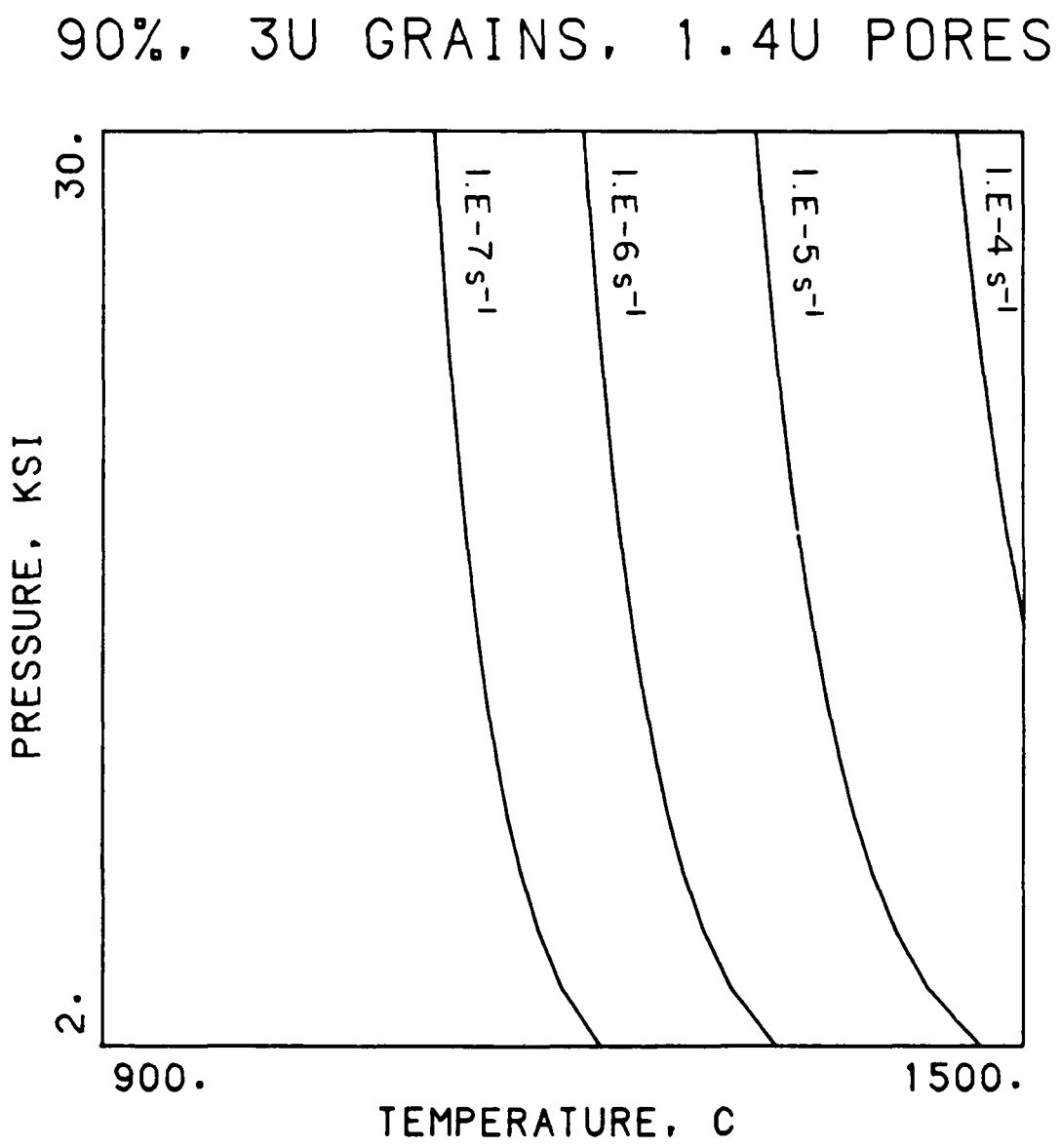

FIGURE 9. DENSIFICATION RATE FOR ALUMINA AT 90% DENSITY. GRAIN SIZE IS 3 μm, PORE SIZE IS 1.4 μm.

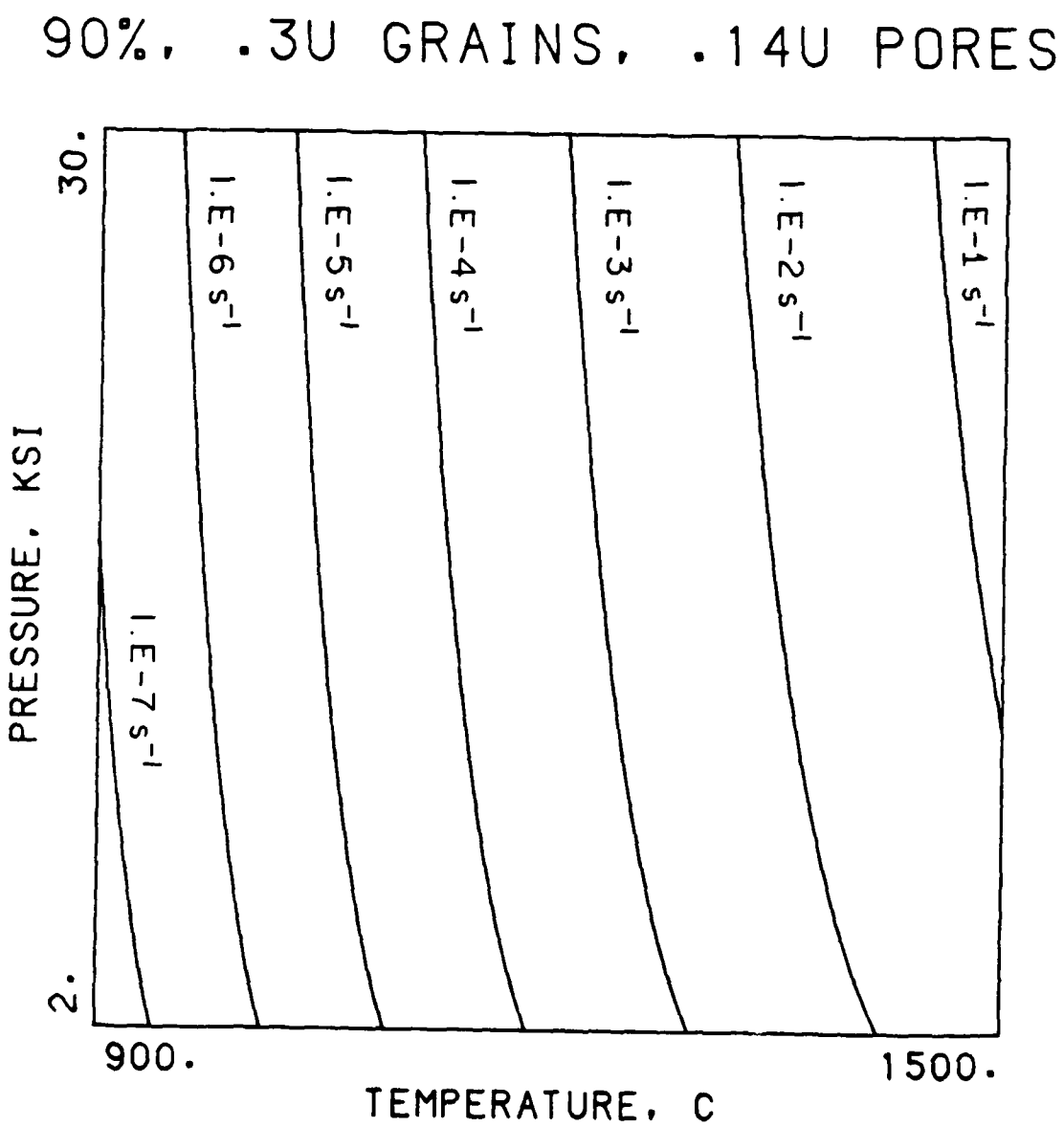

FIGURE 10. DENSIFICATION RATE FOR ALUMINA AT 90% DENSITY. GRAIN SIZE IS 0.3 μm, PORE SIZE IS 0.14 μm.

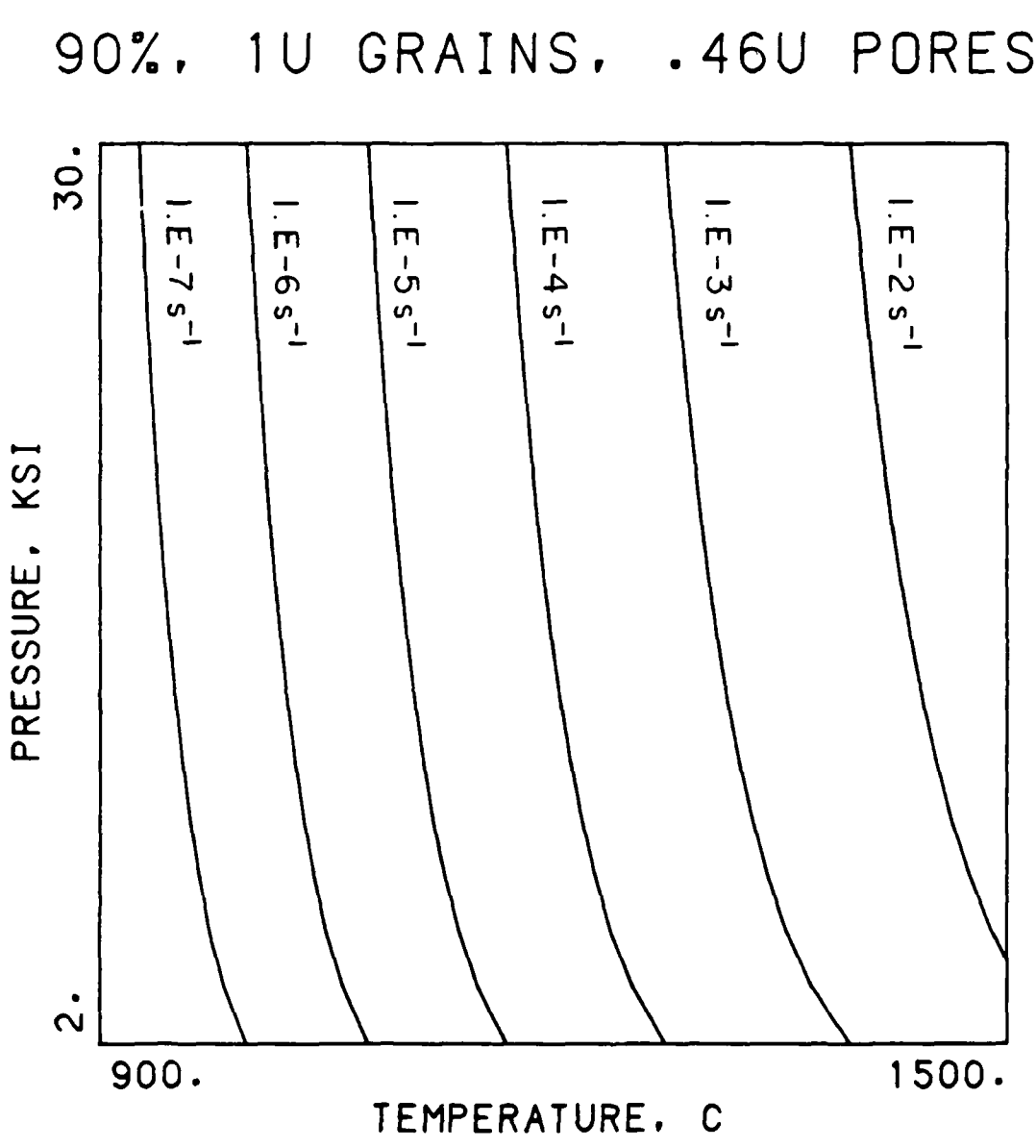

FIGURE 11. DENSIFICATION RATE FOR ALUMINA AT 90% DENSITY. GRAIN SIZE IS 1 μm, PORE SIZE IS 0.46 μm. GRAIN-BOUNDARY DIFFUSIVITY IS TEN TIMES THAT USED TO CALCULATE FIGURES 5 to 10.

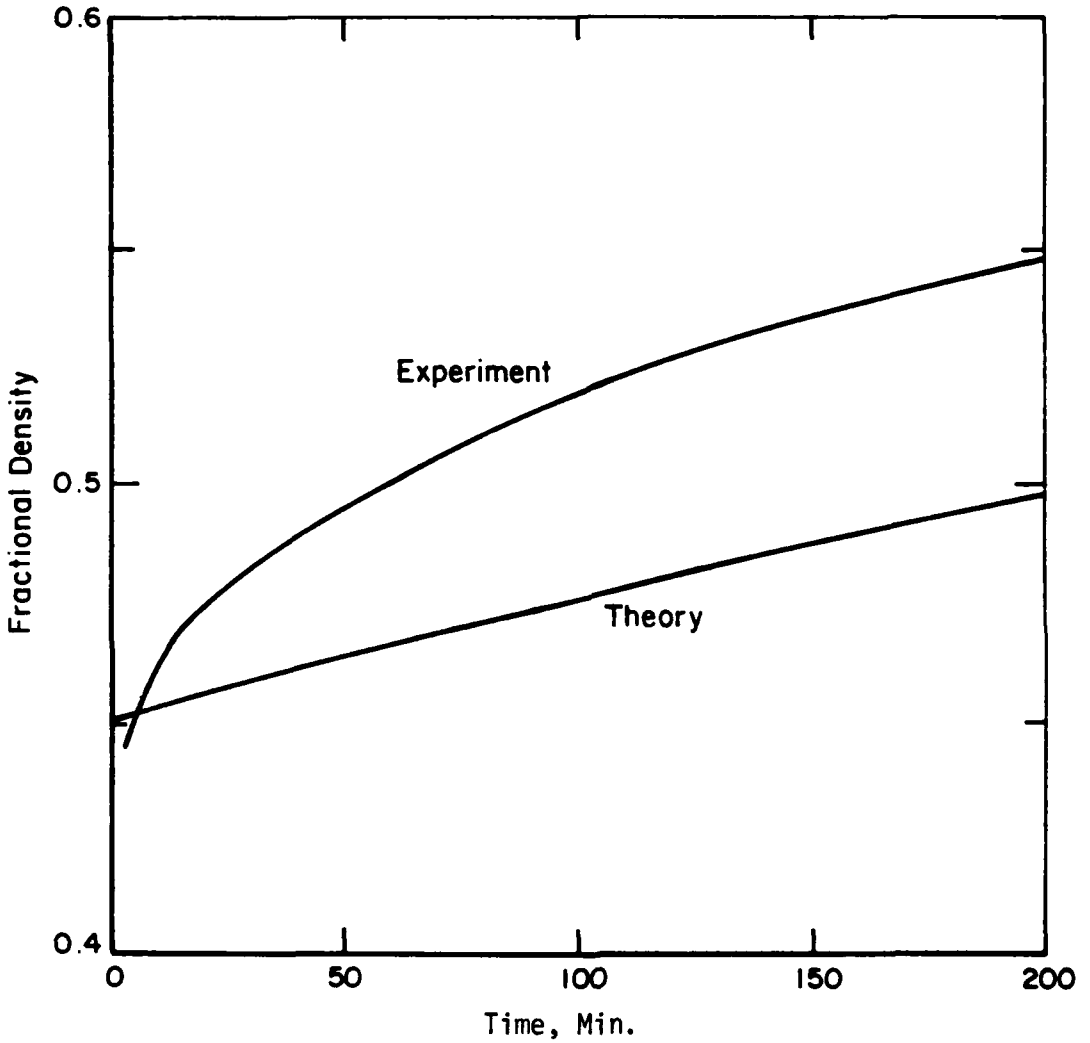

FIGURE 12. COMPARISON OF THEORY WITH DATA OF FELTEN[28] FOR HOT-PRESSING OF 0.3 μm ALUMINA AT 1000°C and 5000 psi.

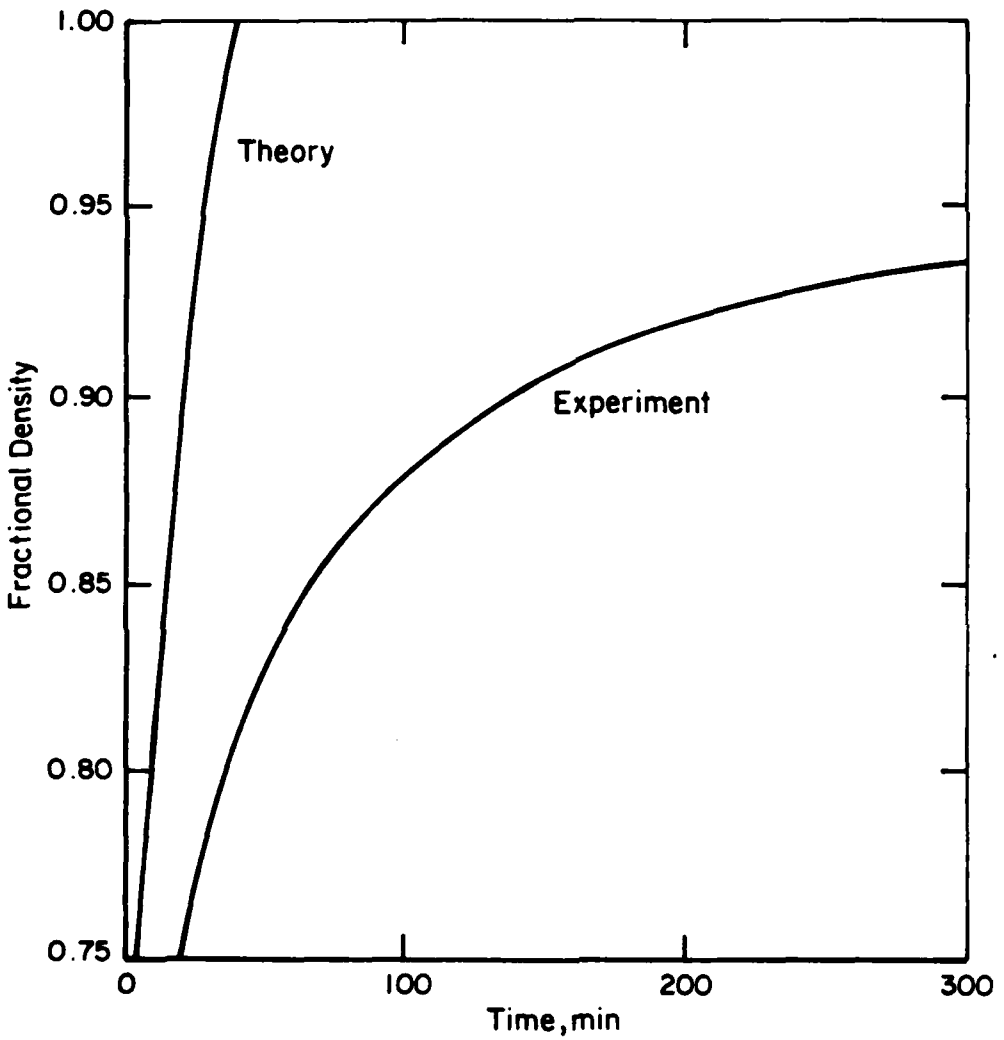

FIGURE 13. COMPARISON OF THEORY WITH DATA OF ROSSI AND FULRATH[26] FOR HOT-PRESSING OF 0.3 μm ALUMINA AT 3000 psi.

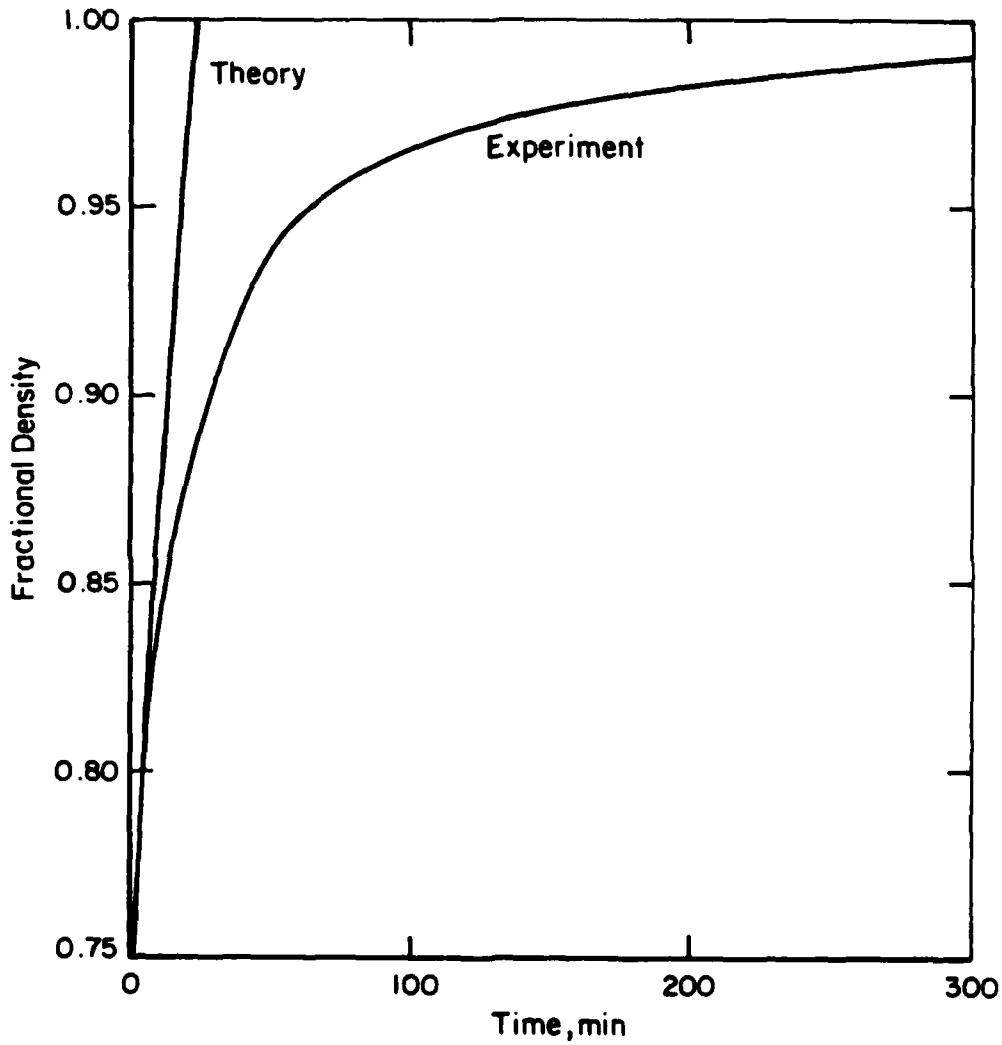

FIGURE 14. COMPARISON OF THEORY WITH DATA OF ROSSI AND FULRATH(26) FOR HOT-PRESSING OF 0.3 μm ALUMINA AT 6000 psi.

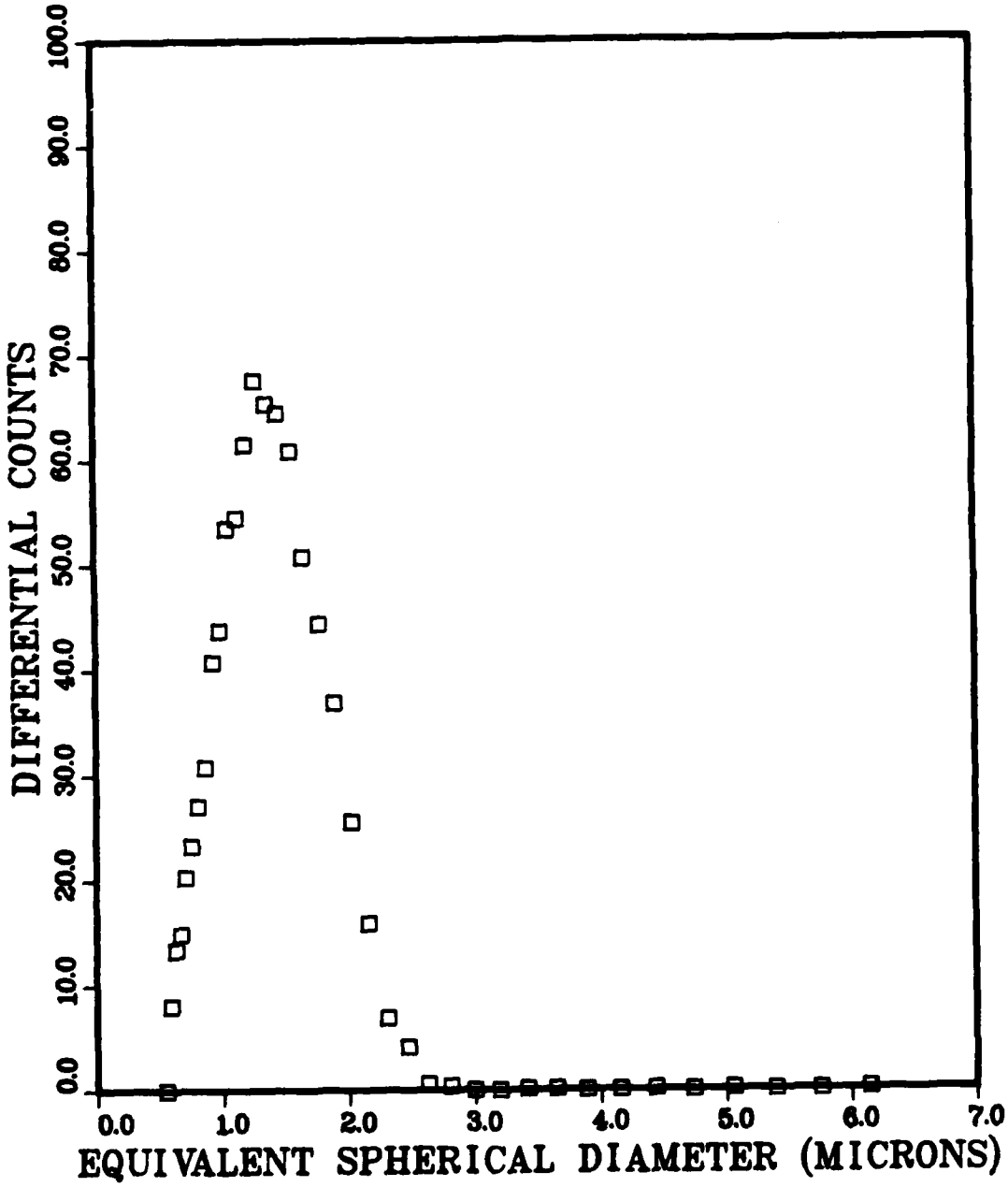

FIGURE 15. DIFFERENTIAL PARTICLE POPULATION AS A FUNCTION OF EQUIVALENT SPHERICAL DIAMETER FOR REYNOLDS RC-HP-DBM ALUMINA WITHOUT MAGNESIA

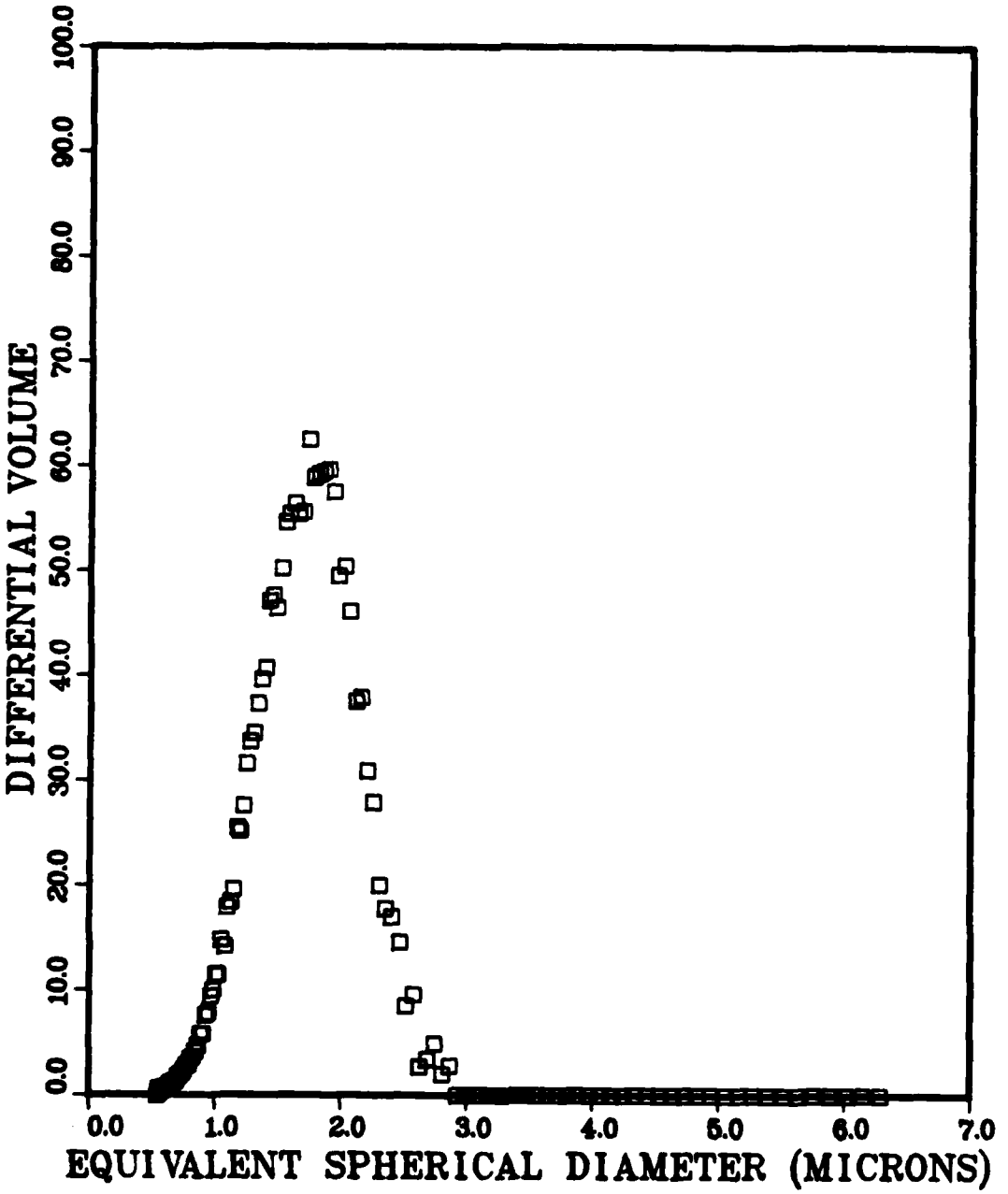

FIGURE 16. DIFFERENTIAL PARTICLE VOLUME AS A FUNCTION OF EQUIVALENT SPHERICAL DIAMETER FOR REYNOLDS RC-HP-DBM ALUMINA WITHOUT MAGNESIA

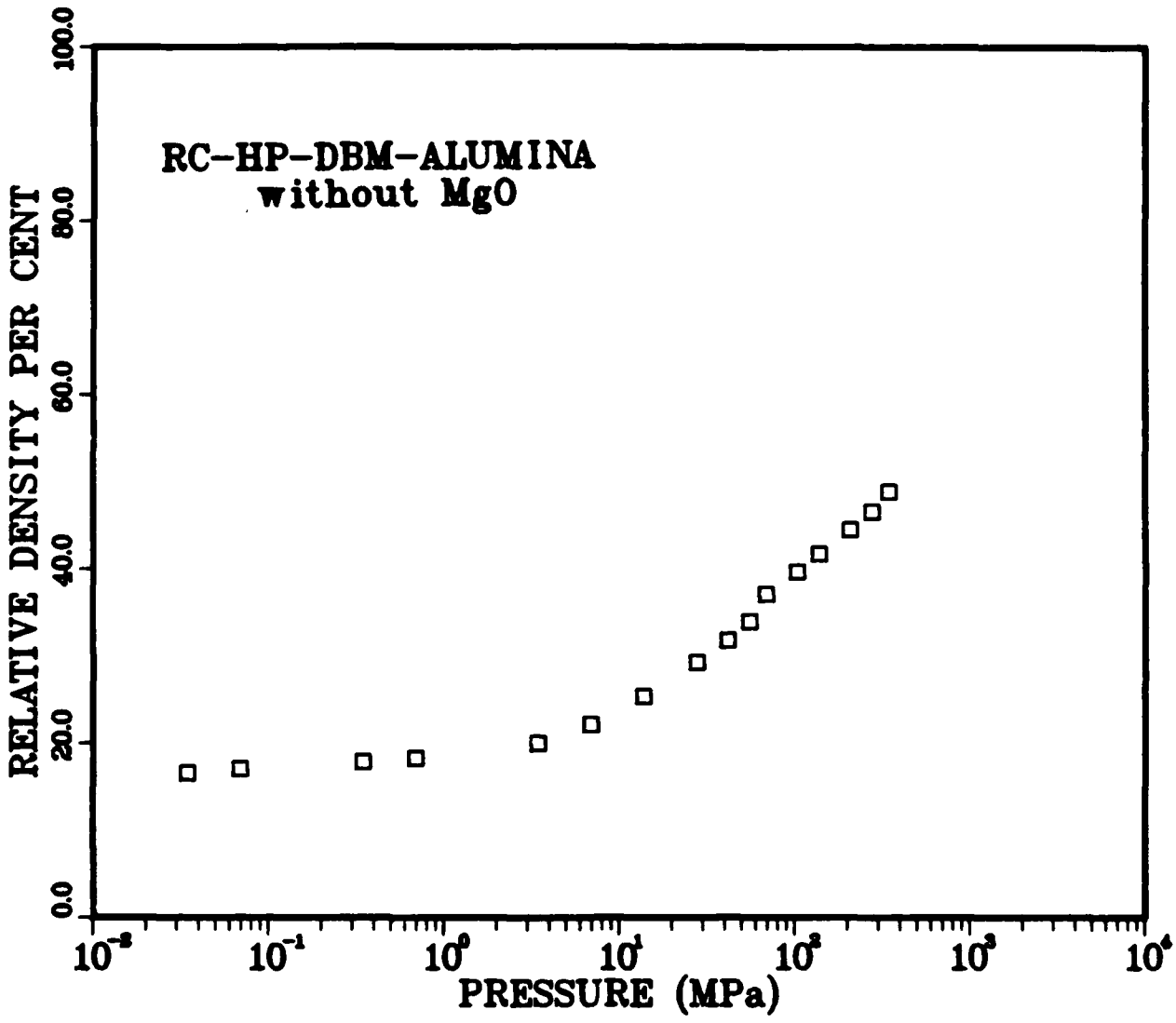

FIGURE 17. COMPACTION CURVE FOR PERCENT THEORETICAL DENSITY VS APPLIED PRESSURE OF REYNOLDS RC-HP-DBM ALUMINA WITHOUT MAGNESIA

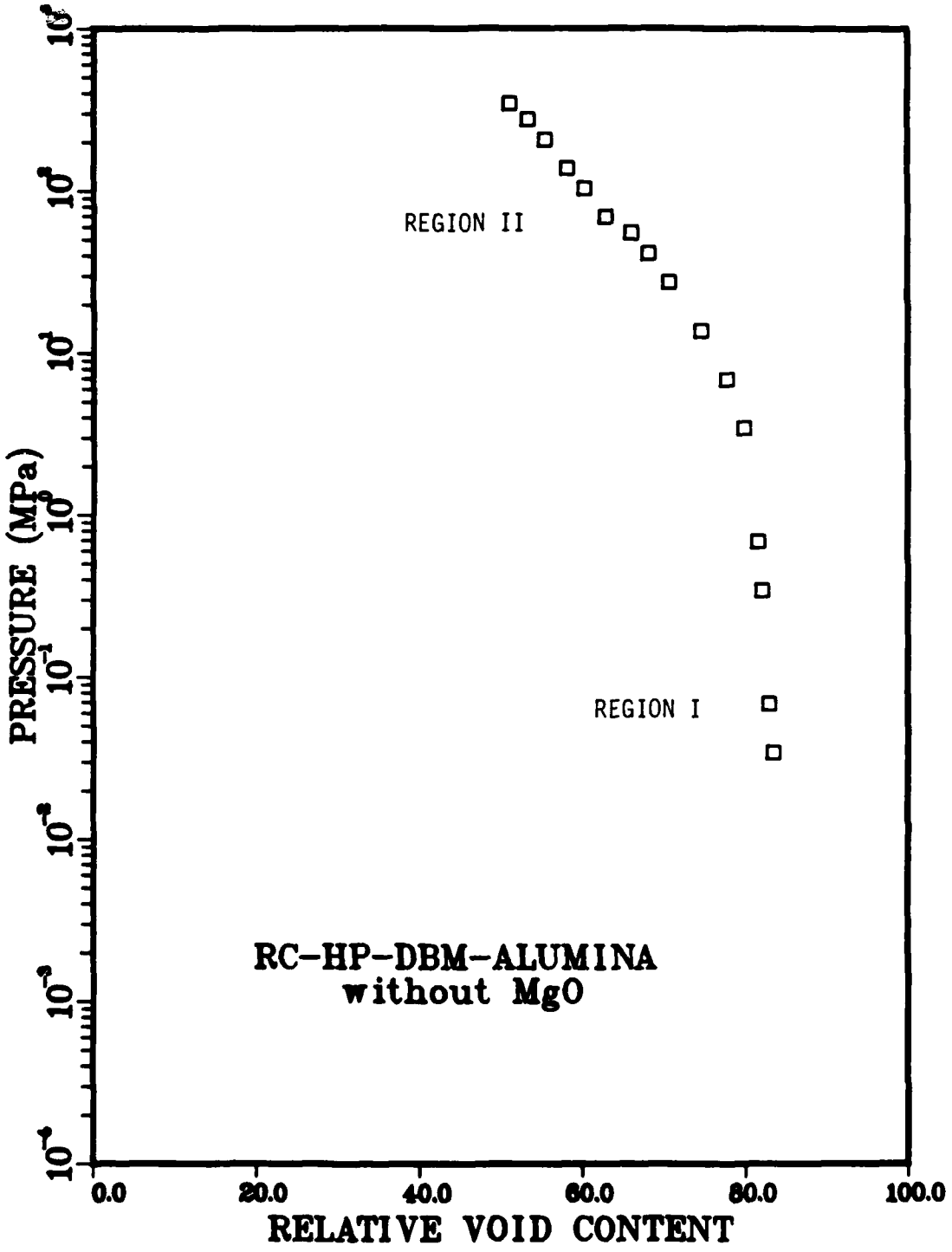

FIGURE 18. DONACHIE-BURR PLOT FOR RELATIVE VOID CONTENT VS APPLIED PRESSURE FOR REYNOLDS RC-HP-DBM ALUMINA WITHOUT MAGNESIA

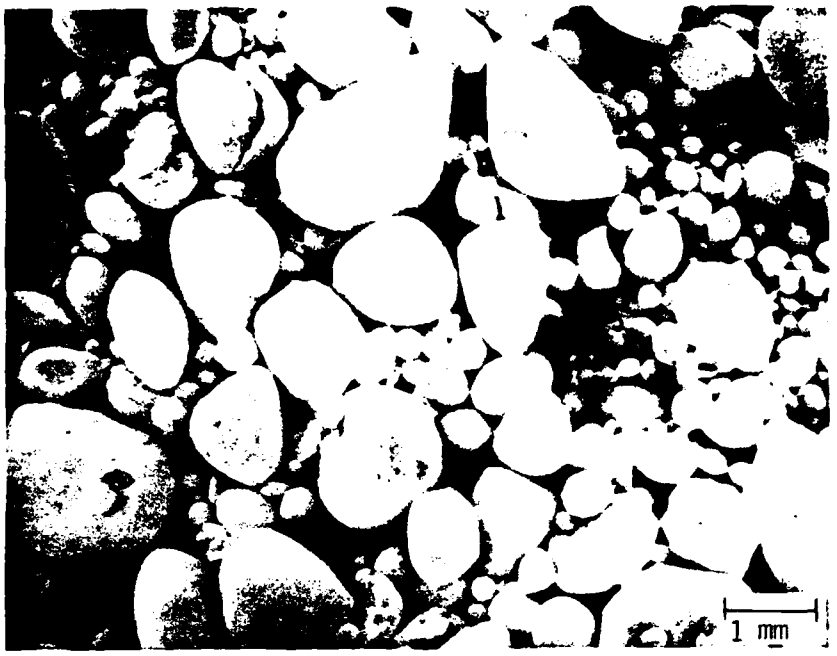

(a)

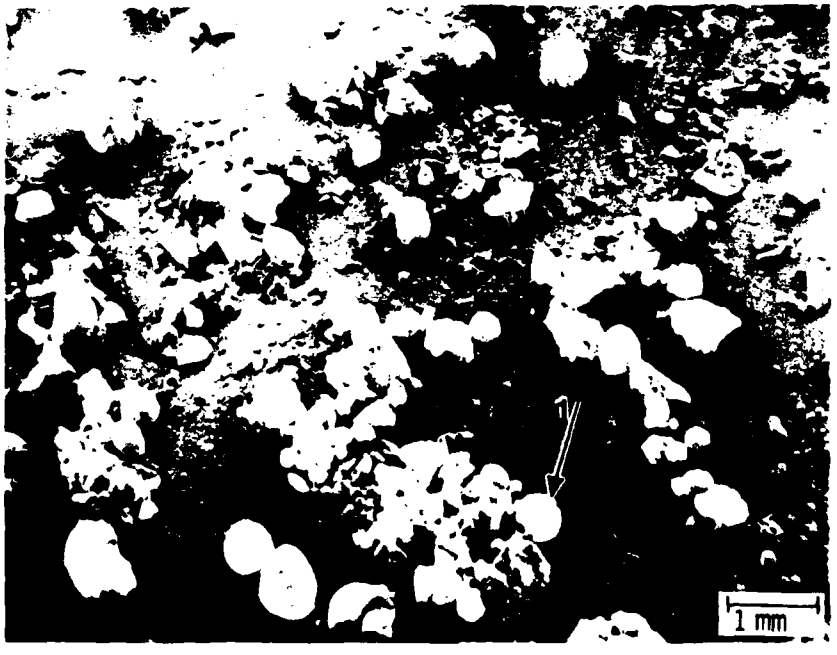

(b)

FIGURE 19. SCANNING ELECTRON PHOTOMICROGRAPH OF REYNOLDS RC-HP-DBM ALUMINA WITHOUT MAGNESIA: 19(a) AS-RECEIVED POWDER (30X); 5(b) POWDER CRUSHED ON SAMPLE HOLDER (30X). SEE FIGURE 21(b) FOR HIGH MAGNIFICATION VIEWS OF AREA 1 IN 19(b).

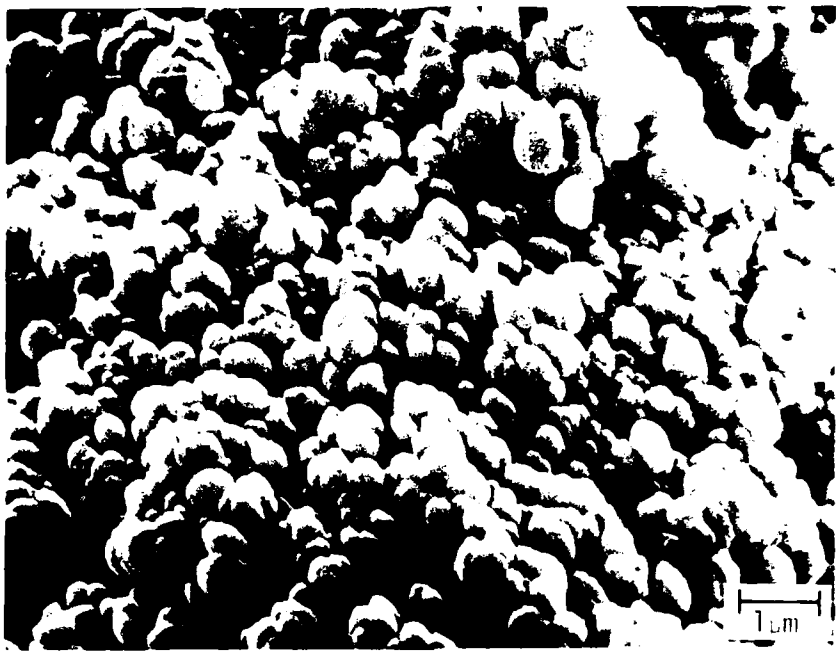

(a)

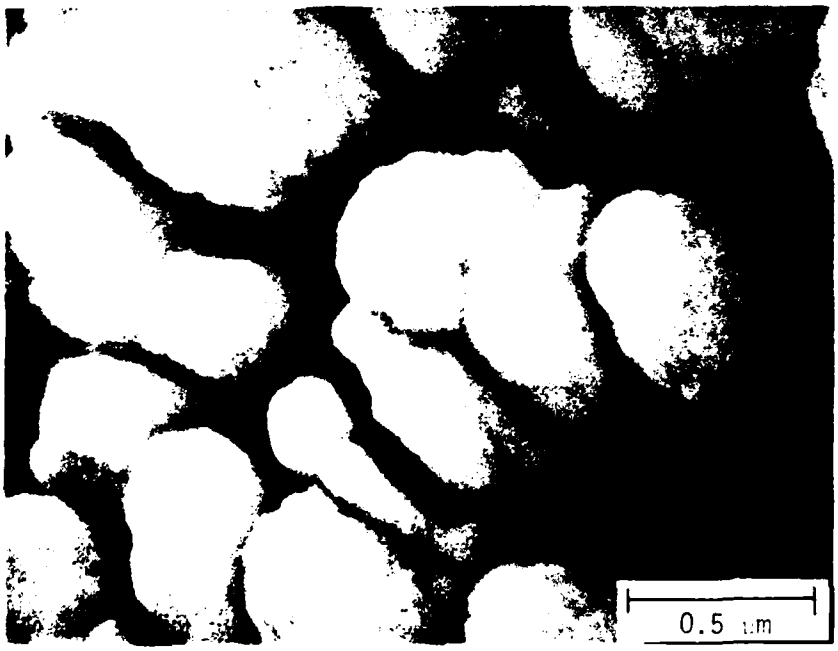

(b)

FIGURE 20. SCANNING ELECTRON PHOTOMICROGRAPHS OF REYNOLDS RC-HP-DBM ALUMINA WITHOUT MAGNESIA: 20(a) 10,000X MAGNIFICATION; 20(b) 50,000X MAGNIFICATION

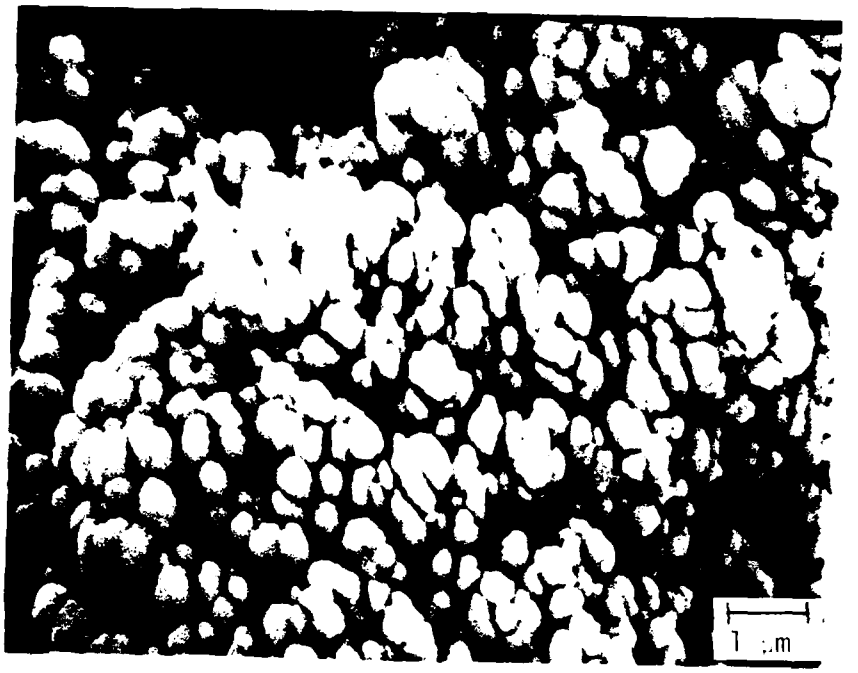

(a)

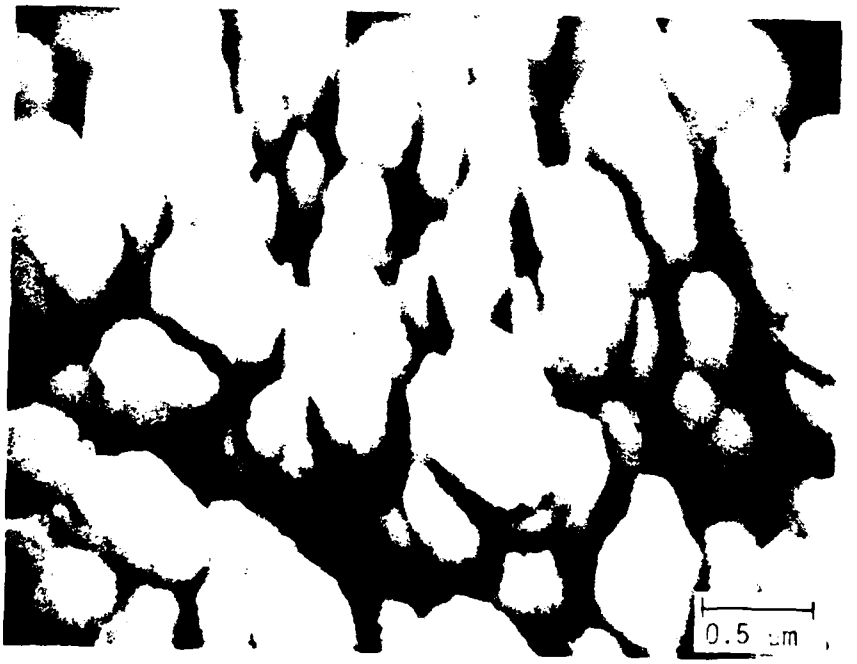

(b)

FIGURE 21. SCANNING ELECTRON PHOTOMICROGRAPHS OF CRUSHED REYNOLDS RC-HP-DBM ALUMINA WITHOUT MAGNESIA: 21(a) 10,000X MAGNIFICATION; 21(b) 30,000X MAGNIFICATION. SEE FIGURE 19(b) FOR LOW MAGNIFICATION VIEW.

IL691 100X

FIGURE 22. PHOTOMICROGRAPH OF HIP SPECIMEN #9, PROCESSED FOR 0 MIN. AT 1100C.

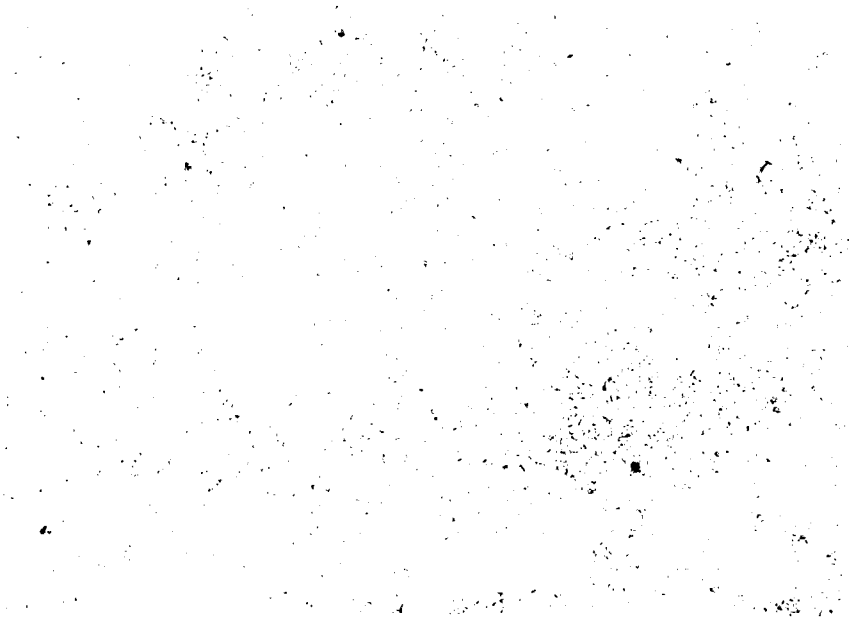

IL693 100X

FIGURE 23. PHOTOMICROGRAPH OF HIP SPECIMEN #11, PROCESSED FOR 15 MIN. AT 1100C.

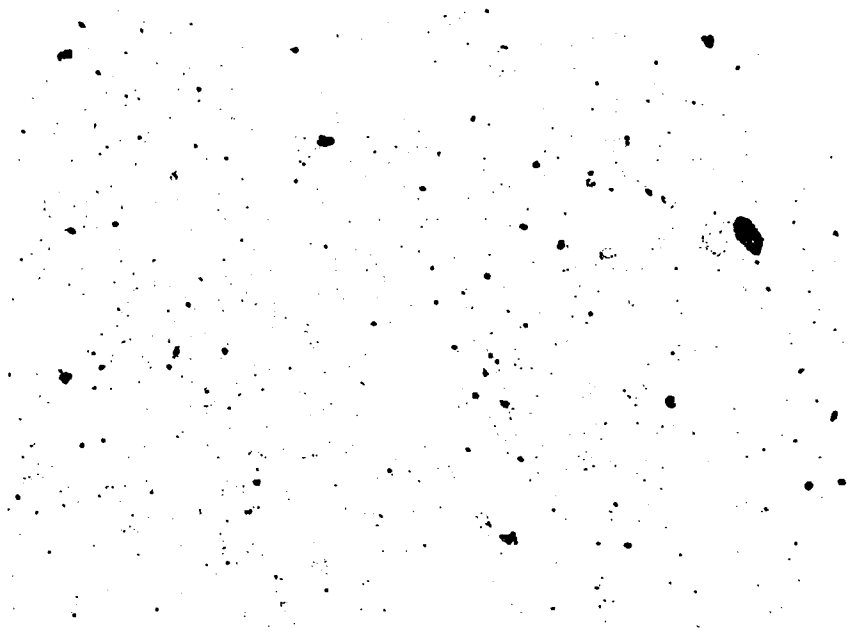

IL694 100X

FIGURE 24. PHOTOMICROGRAPH OF HIP SPECIMEN #12, PROCESSED FOR 30 MIN. AT 1100C.

IL692 100X

FIGURE 25. PHOTOMICROGRAPH OF HIP SPECIMEN #10, PROCESSED FOR 60 MIN. AT 1100C

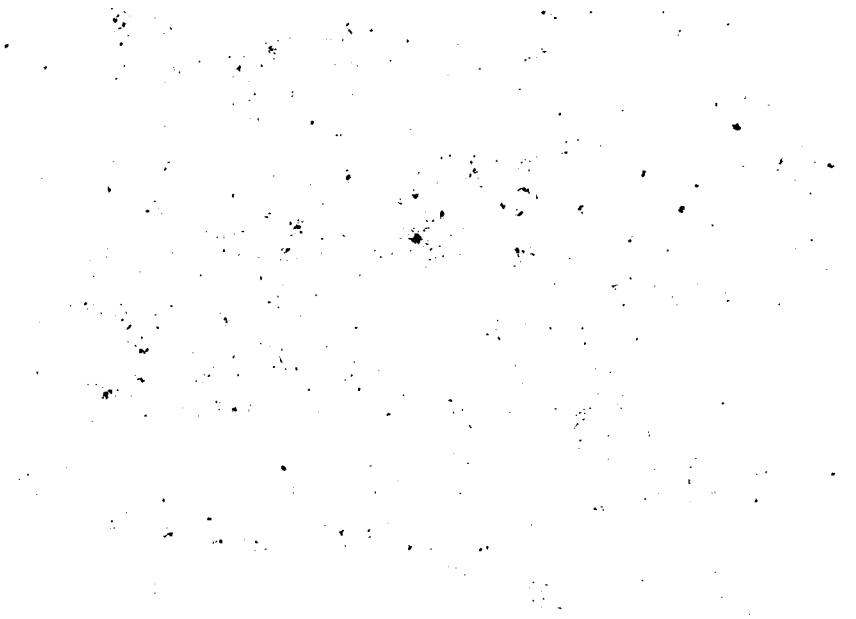

IL690 100X

FIGURE 26. PHOTOMICROGRAPH OF HIP SPECIMEN #7, PROCESSED FOR 180 MIN. AT 1100C.

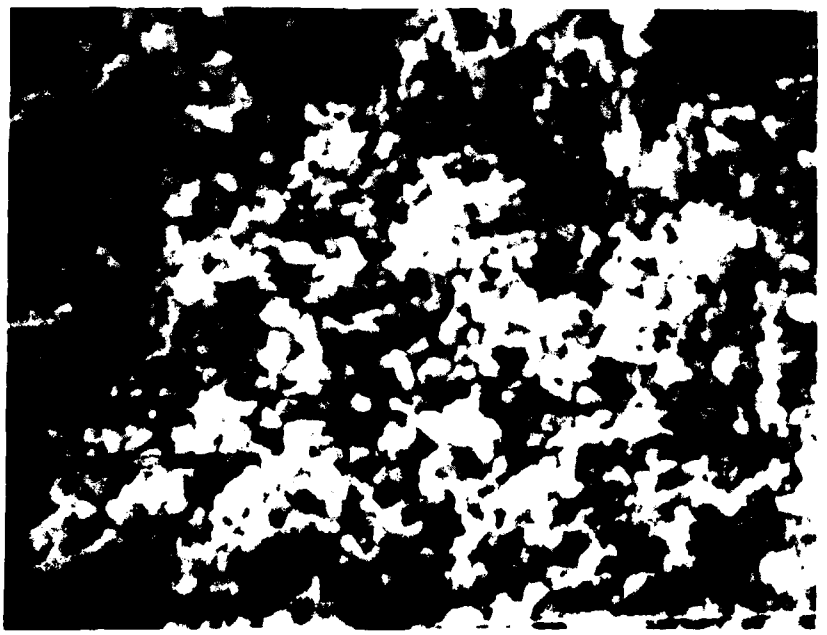

28074A 10,000X

FIGURE 27. SCANNING ELECTRON PHOTOMICROGRAPH OF BISQUE FIRED SPECIMEN, FRACTION SURFACE.

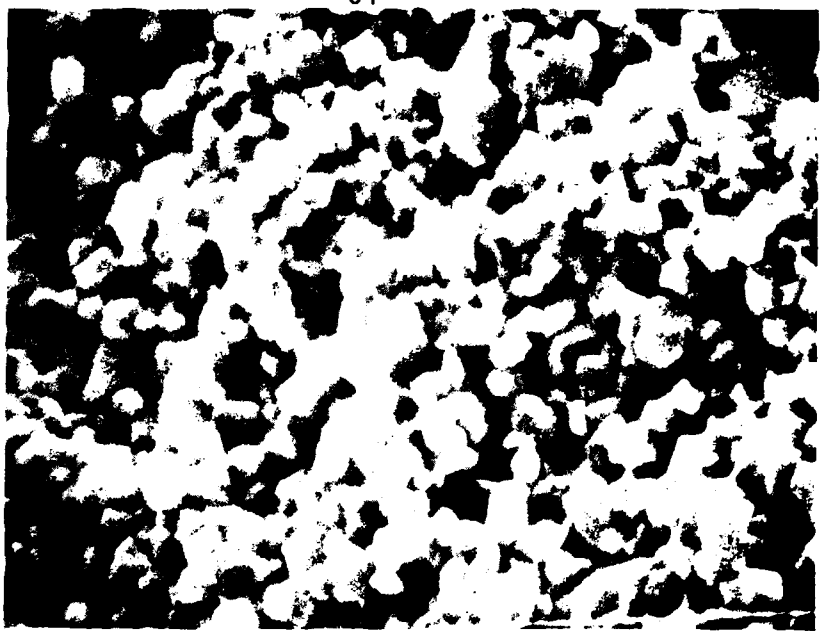

28034A 10,000X

FIGURE 28. SCANNING ELECTRON PHOTOMICROGRAPH OF SPECIMEN #12, FRACTURE SURFRACE. HIP PROCESSED FOR 30 MIN. AT 1100C.

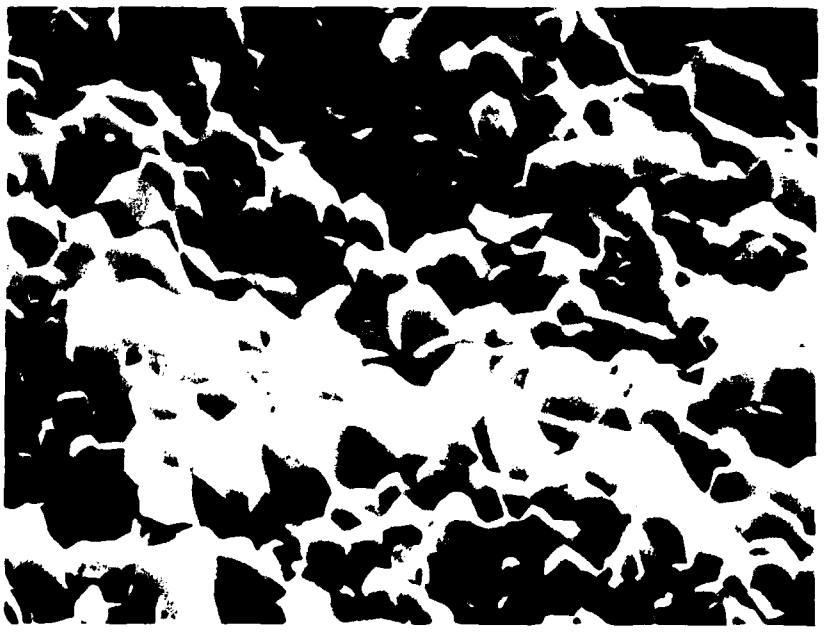

40407 10,000X

FIGURE 29. SCANNING ELECTRON PHOTOMICROGRAPH OF SPECIMEN #7, FRACTURE SURFACE. HIP PROCESSED 180 MIN. AT 1100C.

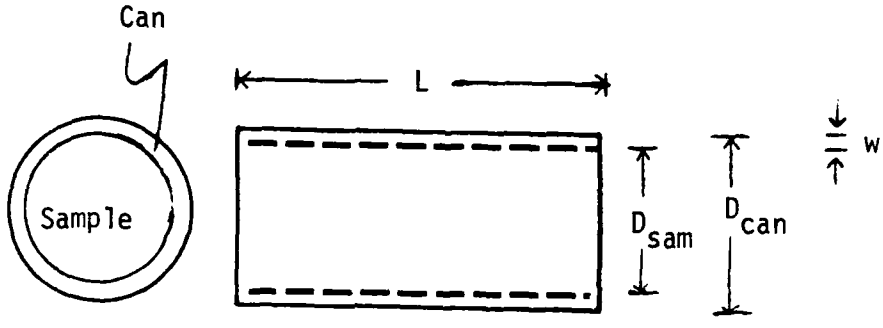

FIGURE 30. SCHEMATIC CAN GEOMETRY

FIGURE CAPTIONS FOR FIGURES 31-34

FIGURE 31. Comparison between experiment and theory. Experimental data include temperature, pressure, and density as functions of time in hours. Points marked "+" are immersion densities. Theoretical density curves were calculated for gas-free pores and fixed grain sizes, as labeled.

FIGURE 32. Comparison between experiment and theory. Experimental data are as in Figure 31. Theoretical density curves were calculated for gas-filled pores and fixed grain sizes, as labeled. Amount of gas in pores produces 1% terminal porosity.

FIGURE 33. Comparison between experiment and theory. Experimental data are as in Figure 31. Theoretical density curves were calculated for gas-free pores and changing grain size as measured from HIP samples. Literature values of diffusivities were multiplied by constants, as labeled, in calculating theoretical curves.

FIGURE 34. Comparison between experiment and theory. Experimental data are as in Figure 31. Theoretical density curves were calculated for gas-filled pores and changing grain size as measured from HIP samples. Literature values of diffusivities were multiplied by constants, as labeled, in calculating theoretical curves. Amount of gas in pores produces 1% terminal porosity as 0.53 micron grain size.

FIGURE 31.

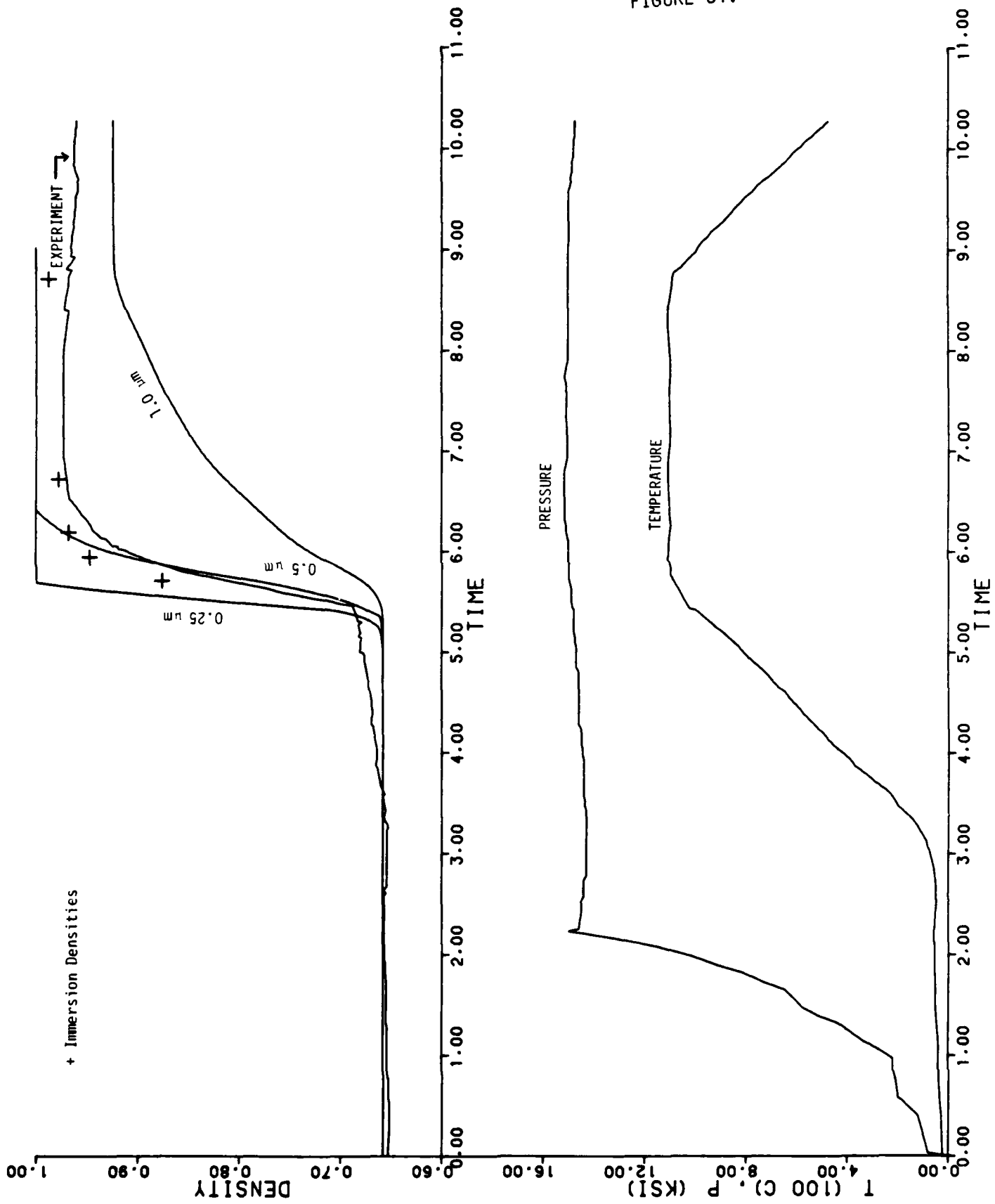
DENSITY
1.00
0.90
0.80
0.70
0.60
0.25 μm
0.5 μm
1.0 μm
EXPERIMENT
+ Immersion Densities
TIME
0.00
1.00
2.00
3.00
4.00
5.00
6.00
7.00
8.00
9.00
10.00
11.00
T (100 C), P (KSI)
16.00
12.00
8.00
4.00
0.00
PRESSURE
TEMPERATURE
TIME

FIGURE 32.

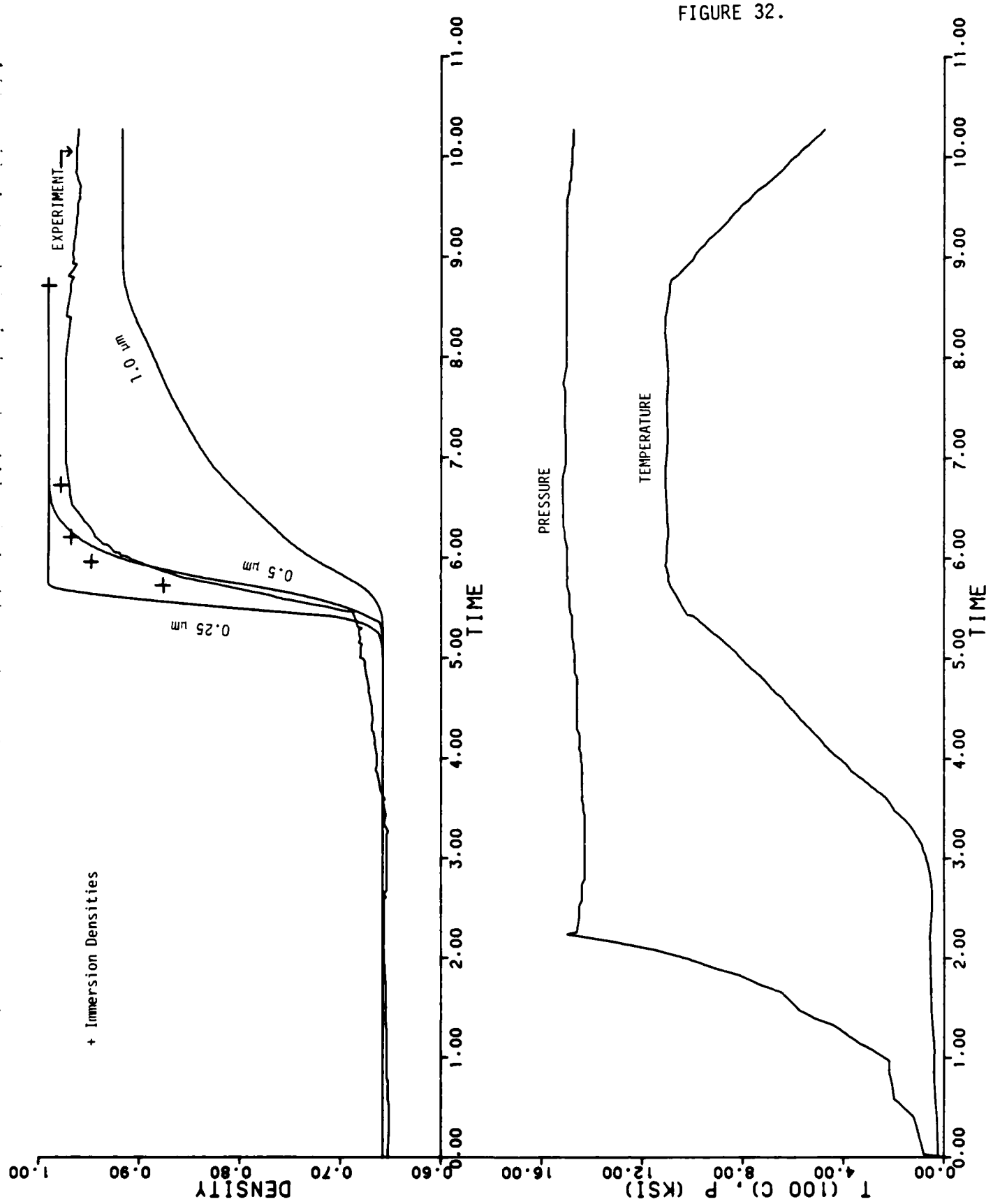
DENSITY
1.00
0.90
0.80
0.70
0.60
0.00
1.00
2.00
3.00
4.00
5.00
6.00
7.00
8.00
9.00
10.00
11.00
TIME
EXPERIMENT
1.0 μm
0.5 μm
0.25 μm
+ Immersion Densities
T (100 C), P (KSI)
16.00
12.00
8.00
4.00
0.00
PRESSURE
TEMPERATURE

FIGURE 33.

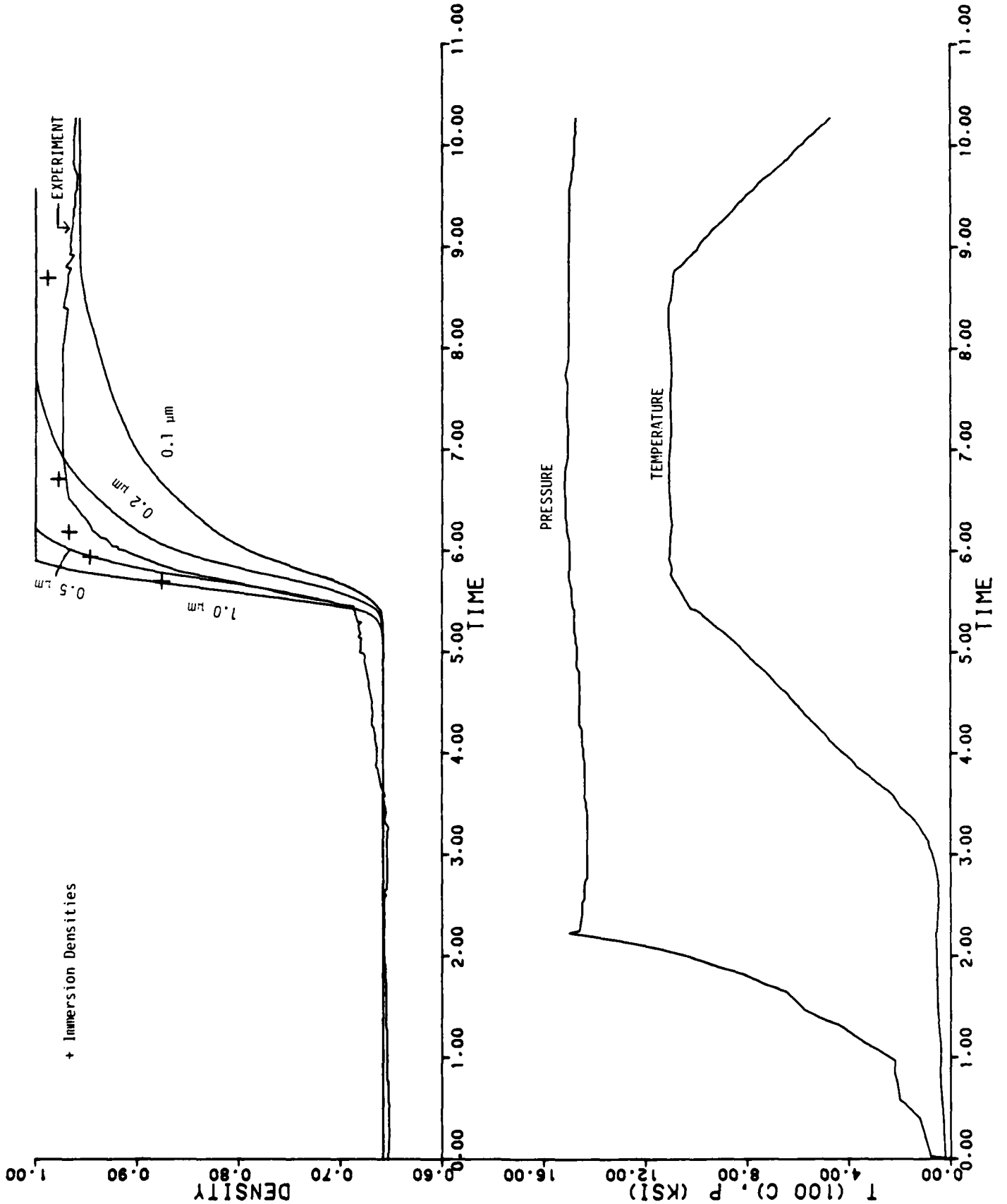
DENSITY
1.00
0.90
0.80
0.70
0.60
TIME
0.00
1.00
2.00
3.00
4.00
5.00
6.00
7.00
8.00
9.00
10.00
11.00
EXPERIMENT
0.1 μm
0.2 μm
0.5 μm
1.0 μm
+ Immersion Densities
T (100 C), P (KSI)
16.00
12.00
8.00
4.00
0.00
PRESSURE
TEMPERATURE
TIME

FIGURE 34.

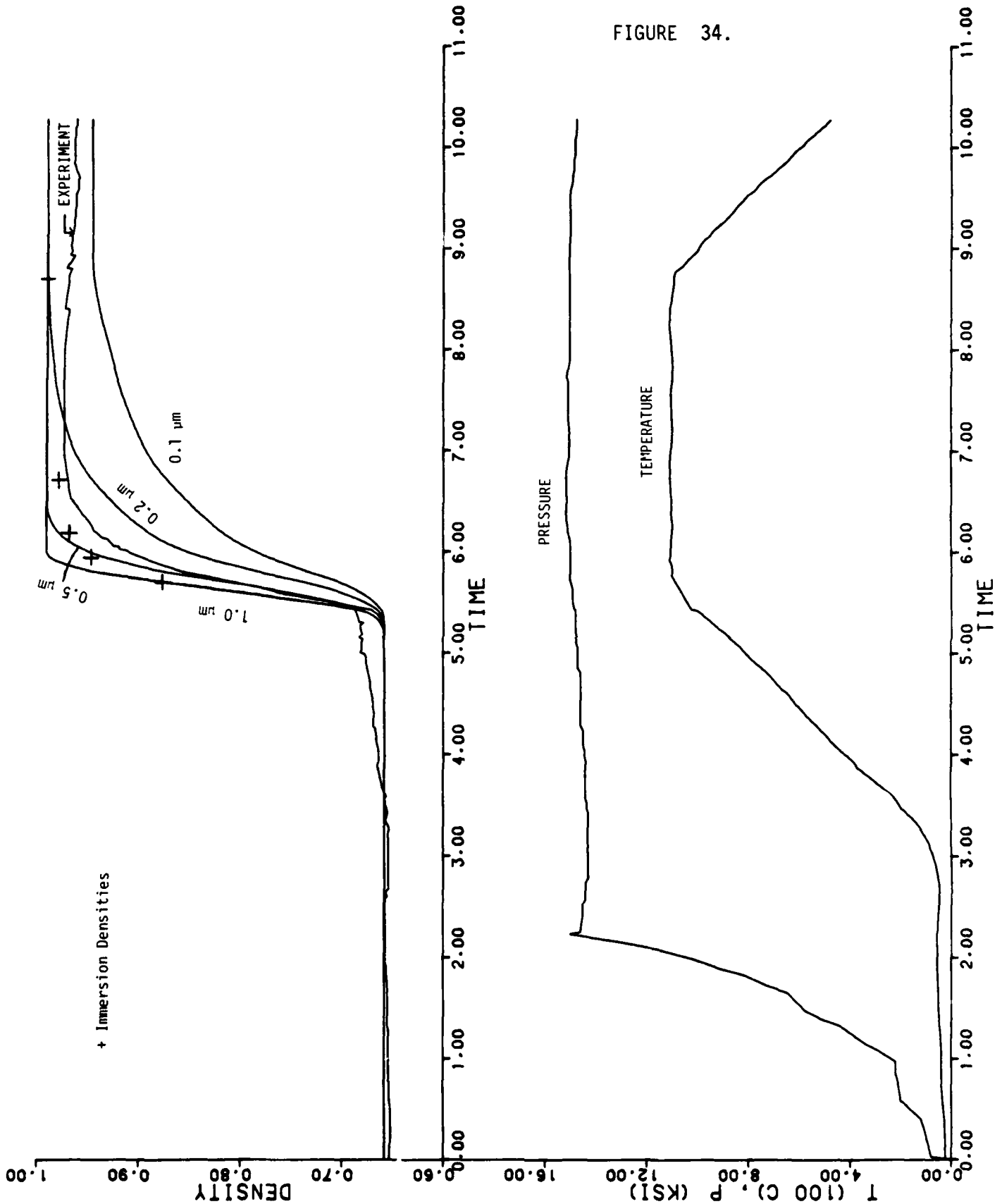
DENSITY
1.00
0.90
0.80
0.70
0.60
+ Immersion Densities
EXPERIMENT
0.1 μm
0.2 μm
0.5 μm
1.0 μm
TIME
0.00
1.00
2.00
3.00
4.00
5.00
6.00
7.00
8.00
9.00
10.00
11.00
T (100 C), P (KSI)
16.00
12.00
8.00
4.00
0.00
PRESSURE
TEMPERATURE

REFERENCES

1. H.A. Saller, S.J. Paprocki, R.W. Dayton and E.S. Hodge, "A Method of Bonding", U.S. Patent No. 687-842 and Canadian Patent No. 680, 160, February 1964.

2. R.R. Wills and M.C. Brockway, "Hot Isostatic Pressing of Ceramics", Proc. Brit. Ceram. Soc. 31 233 (1981).

3. J. Weertman and J.R. Weertman, "Mechanical Properties, Strongly Temperature Dependent", in Physical Metallurgy , pp. 793-819, ed. R.W. Cahn, North Holland, Amsterdam, 1965.

4. E. Arzt, M.F. Ashby, and K.E. Easterling, "Practical Applications of Hot Isostatic Pressing Diagrams: Four Case Studies", Met. Trans. A 14 211 (1983).

5. A.H. Heuer, N.J. Tighe and R.M. Cannon, "Plastic Deformation of Fine-Grained Alumina (Al_2O_3): II, Basal Slip and Nonaccommodated Grain-Boundary Sliding", J. Am. Ceram. Soc., 63 53 (1980).

6. D.M. Kotchick and R.E. Tressler, "Deformation Behavior Sapphire via the Prismatic Slip System", J. Am. Ceram. Soc., 63 429 (1980).

7. J.P. Hirth and J. Lothe, Theory of Dislocations, pp 276-286, McGraw-Hill, New York, 1968.

8. M.L. Kronberg, "Dynamical Flow Properties of Single Crystals of Sapphire, I", J. Am. Ceram. Soc. 45 274 (1962).

9. W.R. Cannon, "Mechanisms of High Temperature Creep in Polycrystalline Al_2O_3", Ph.D. Thesis, Stanford University, 1971.

10. F.A. Mohamed and T.G. Langdon, "Recent Development in Deformation Mechanism Maps for Ceramics", in Ceramic Microstructures '76, pp 763-773, ed. R.M. Fulrath and J.A. Pask, Westview, Boulder, Colorado, 1976.

11. R.M. Cannon and R.L. Coble, "Review of Diffusional Creep of Al_2O_3", in Deformation of Ceramic Materials pp. 61-100, ed. K.C. Bradt and R.E. Tressler, Plenum, New York, 1975.

12. A.E. Paladino and W.D. Kingery, "Aluminum ion Diffusion in Aluminum Oxide", J. Chem. Phys. 37 957 (1962).

13. Y. Oishi and W.D. Kingery, "Self-Diffusion of Oxygen in Single Crystal and Polycrystalline Aluminum Oxide", J. Chem. Phys. 33 480 (1960).

14. R.M. Cannon, W.H. Rhodes, and A.H. Heuer, "Plastic Deformation of Fine-Grained Alumina (Al_2O_3): I, Interface-Controlled Diffusional Creep", J. Am. Ceram. Soc. 63 46 (1980).

REFERENCES (Continued)

15. M.F. Ashby, "On Interface-Reaction Control of Nabarro-Herring Creep and Sintering", Scripta Met. 3 837 (1969).

16. B. Burton, "Interface Reaction-Controlled Diffusional Creep, A Consideration of Grain-Boundary Dislocation Climb Sources", Mater. Sci. Eng. 10 9 (1972).

17. A.J. Markworth, "Volume Diffusion Controlled Final Stage Densification of a Porous Solid", Scripta Met. 6 957 (1972).

18. E. Ryshkewitch, "Rigidity Modulus of Some Pure Oxide Bodies - 8th Communication to Ceramography", J. Am. Ceram. Soc. 34 322 (1951).

19. N. Soga and O.L. Anderson, "High-Temperature Elastic Properties of Polycrystalline MgO and Al_2O_3", J. Am. Ceram. Soc. 49 356 (1966).

20. D.S. Wilkinson and M.F. Ashby, "The Development of Pressure-Sintering Maps", in Materials Science Research Volume 10: Sintering and Catalysis, pp. 473-492, ed. G.C. Kuczynski, Plenum, New York, 1975.

21. R.L. Coble, "Diffusion Models for Hot-Pressing with Surface Energy and Pressure Effects as Driving Forces", J. Appl. Phys. 41 4798 (1970).

22. D.S. Wilkinson and M.F. Ashby, "Pressure Sintering by Power-Law Creep", Acta. Met. 23 1277 (1975).

23. J.K. McCoy, "A Rational Method for Calculating Mechanism Maps", Scripta Met. 17 563 (1983).

24. G.M. Fryer, "Pressure-Sintering of Alumina", Trans. Brit. Ceram. Soc. 68 185 (1969).

25. R.C. Rossi, J.D. Buch, and R.M. Fulrath, "Intermediate-Stage Densification in Vacuum Hot-Pressing of Alumina", J. Am. Ceram. Soc. 53 629 (1970).

26. R.C. Rossi and R.M. Fulrath, "Final-Stage Densification in Vacuum Hot-Pressing of Alumina", J. Am. Ceram. Soc. 48 558 (1965).

27. S. Sclosa, D.F. Dailly, and G.W. Hastings, "Fracture Toughness of Hot Isostatically Pressed Alumina", Trans. J. Brit. Ceram. Soc. 81 148 (1982).

28. E.J. Felten, "Hot Pressing of Alumina Powders at Low Temperatures", J. Am. Ceram. Soc. 44 381 (1961).

REFERENCES (Continued)

29. M.J. Donachie and M.F. Burr, J. Met., 15 849-855 (1963).

30. Y.S. Touloukian, Thermophysical Properties of High Temperature Solid Materials, V. 3, pp. 211-212, V. 4, pp. 22-25, Macmillan, New York, 1967.

31. W.D. Kingery, Introduction to Ceramics, p. 359, Wiley, New York, 1960. Kingery's Eq. 12.9 is shown incorrectly integrated in Ea. 12.10.

APPENDIX A

A RATIONAL METHOD FOR CALCULATING MECHANISM MAPS

J. Kevin McCoy

Battelle, Columbus Laboratories
505 King Avenue
Columbus, Ohio 43201, U.S.A.

SUMMARY

A coherent algorithm is presented for the calculation and plotting of mechanism maps. The method has three significant advantages: (1) The number of points at which deformation rates are evaluated is greatly reduced, providing computational efficiency, (2) the method is applicable to any map, not just those in which the contours and boundaries can be represented by straight lines, and (3) the maps are plotted in essentially report-ready form, minimizing the need for hand drafting. Examples of maps generated by this method are given.

1. INTRODUCTION

Since the introduction of mechanism maps by Weertman and Weertman [1] and their subsequent development by Ashby [2], there has been a great and growing interest in the construction and use of such maps. They have been used to describe the kinetics of creep [2,3], hot pressing [4], sintering [5], and fracture [6]. In addition, potential-pH diagrams [7], which are constructed in a similar way, have been used

to describe the corrosion behavior of a large number of materials. The discussion in this paper is couched in terms of deformation modeling, but the methods may be applied readily to other problems.

A variety of algorithms have been used in the construction of these maps, but for the present discussion, it will suffice to classify them as "linear" or "point-by-point". The linear methods rely on the use of straight lines to represent the contours and boundaries in the map, with, in some cases, the use of a change of variables to produce the necessary linearization [8]. The point-by-point methods, on the other hand, avoid the assumption of linearity by making an exhaustive scan of the whole map. The point-by-point approach is often thought of as being inefficient because past programs required the evaluation of rates at a large number of points, while linear methods involve the treatment of a linear system at relatively few points. For metallurgical processes, however, it is not clear that linearization is always possible, so it is natural to choose the more general point-by-point approach.

Unfortunately, the point-by-point programs which were available to us were less than inspiring. They did not meet modern standards of modularity, documentation, or user convenience, and they appeared to be slipshod in their use of data. A review of the literature further suggested that no study had been made of the methods necessary for systematic calculation and plotting of mechanism maps. Accordingly, we set out to develop methods which make careful use of

all data and which could be used to plot maps in essentially final form. Besides the intended advantage of producing finished maps, we also found that our algorithm is surprisingly efficient and requires far fewer points than other point-by-point methods.

2. CALCULATION OF BOUNDARIES

Let us state the problem of the construction of a mechanism map in abstract terms. We have n functions f_i, i=1, n, each of which is dependent on two variables. At any point (x,y), the value $f_i(x,y)$ is the rate of deformation via the ith mechanism. The map describes a rectangular region $x_{min} \leq x \leq x_{max}$, $y_{min} \leq y \leq y_{max}$. The first step in the construction of the map is to divide the map into one or more regions where $f_i(x,y) > f_j(x,y)$ for all $j \neq i$. Such a region will be called a region of dominance of mechanism i. The second step is to find a set of contour lines for each of the regions. The third step is to plot the boundaries of the regions and the contours in a smooth and efficient manner. In the remainder of this paper we will discuss each of these three steps in sequence. Finally, we will present examples which illustrate the efficiency of the algorithm.

To make the problem tractable, a regular grid is superimposed on the map, dividing the area of the map into rectangles. The density of the grid will vary from one map to another, based on the complexity of the map, the desired level of smoothness of the curves, and the need for computational speed.

In calculating the map, each rectangle is treated separately, and the portion of any boundary or contour which lies within the rectangle is represented by a line segment. The general efficiency of the algorithm may be improved by careful storage of the data. It is desirable to evaluate the functions f_i only once at each grid point and to save the results of the analysis of individual sides of a rectangle for subsequent use in analysis of adjacent rectangles.

Since each rectangle is treated separately, let us consider the determination of the boundaries of the regions of dominance which fall within one rectangle. We will first discuss the topology of the boundaries, then investigate how the topology and positions of the boundaries may be calculated.

Figure 1 shows four topologically distinct arrangements of boundaries between regions of dominance in one rectangle of the map. We have found that real mechanism maps very rarely require more complex topologies.

In calculating the positions of the boundaries, no data are used except the values of the functions f_i at the four corners of the rectangle. All boundaries within the rectangle are assumed to be line segments.

Rather than analyzing the rectangle as a whole, we study each side individually, then combine the results for the four sides. We assume that the rates of the various mechanisms vary linearly along the sides of the rectangle. Therefore, if one mechanism is dominant at both

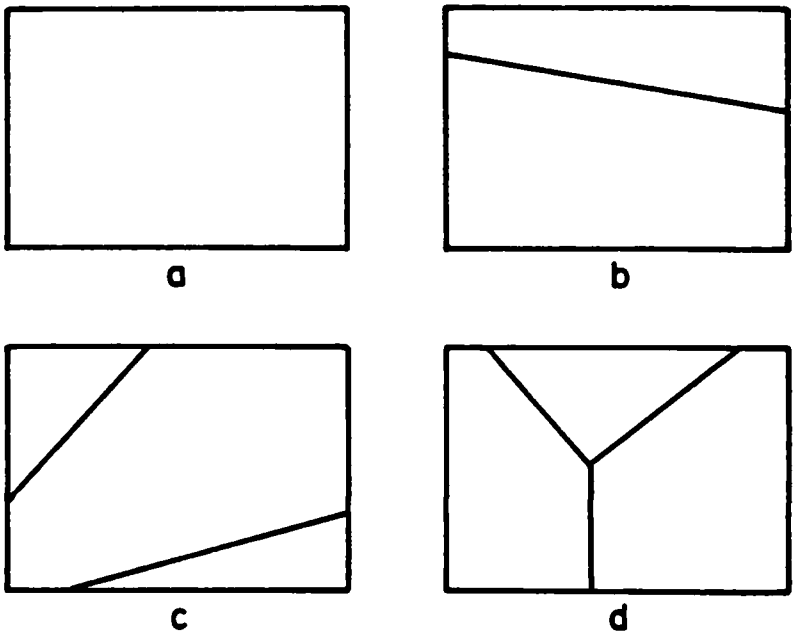

Fig. 1. Four Possible Topologies for Boundaries in One Rectangle of the Map

a. No boundaries, b. One boundary,
c. Two nonintersecting boundaries,
d. Three intersecting boundaries.

ends of a side, it is dominant over the entire side. If two different mechanisms are dominant at the two ends, there are two or three dominant mechanisms on the side, and the points where the boundary or boundaries intersect the side may be calculated using a linear interpolant. Sides with four or more dominant mechanisms can be ignored because of the assumption that only the four topologies of Figure 1 are present.

The topology of the rectangle may be determined by simply adding the number of points where boundaries intersect the four sides of the rectangle. Plotting is trivial if there are zero or two such points. If the boundaries intersect the sides of the rectangle at four points (two nonintersecting boundaries), it is only necessary to draw the boundaries between appropriate pairs of points. If the boundaries intersect the sides of the rectangle at three points (three intersecting boundaries), plotting cannot be done until the location of the intersection is found. In this case, we temporarily treat the rectangle as if only two dominant mechanisms were present, so that the boundary goes all the way across the rectangle. The three line segments obtained will intersect at three points, the centroid of which is used as the intersection of the three boundaries. This procedure is illustrated in Figure 2. The point of intersection could be calculated directly by using a bilinear interpolant and solving for the point at which all three mechanisms have equal rates.

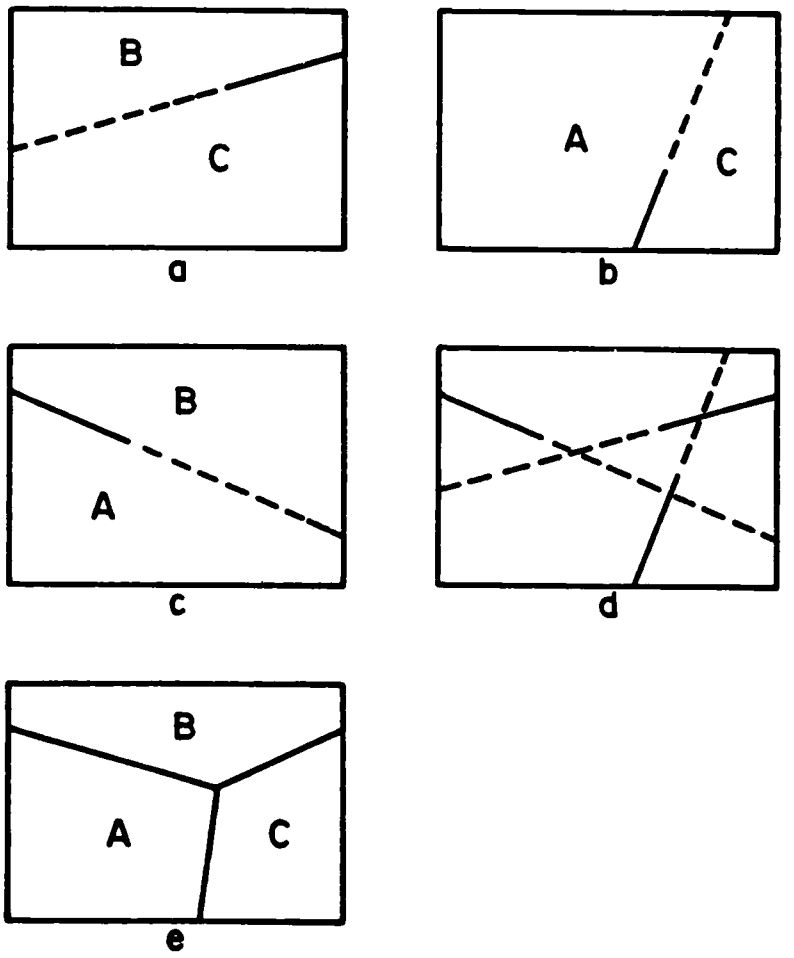

Fig. 2. Treatment of Three Intersecting Boundaries

a,b,c. Location of single boundary if third mechanism were absent. Dotted portion of boundary will be cut off by third mechanism. d. Superposition of a, b, and c. Due to approximations, boundaries do not intersect at a single point. e. Composite map with regions of dominance labeled. Intersection is drawn at centroid of middle triangle in d.

3. CALCULATION OF CONTOURS

Let us now consider the methods used in calculating the positions of the contours of constant deformation rate. First we will consider the case where the entire rectangle lies within a single region of dominance, then we will see how the procedure must be modified to treat cases in which the rectangle is divided between two or more regions of dominance.

In either case, the first step in contouring is to find out which contours will pass through the rectangle. To do this, we must find the minimum and maximum rates of the dominant mechanism(s). If a single mechanism is dominant throughout the rectangle, it is only necessary to check for extrema at the four corners. If there are two or more dominant mechanisms, it is also necessary to check the rates at the points where the boundaries intersect the sides of the rectangle and, if there is such a point, where three boundaries intersect. Given the minimum and maximum rate, the minimum and maximum contour levels follow immediately.

For the case in which a single mechanism is dominant throughout the rectangle, we first search all four sides of the rectangle for points where the rate of the dominant mechanism is the same as a contour level. There will be either two or four such points. If there are two points, the contour is taken to be the line segment which connects the points. If there are four points, a more or less arbitrary criterion must be used to decide which pairs of points will be connected by contours.

For the case in which two or more mechanisms are dominant in different portions of the rectangle, each mechanism is contoured individually as if it were dominant throughout the rectangle. The contour segments are then "cut to length" by truncating them at the point where they enter a different region of dominance.

4. SORTING AND PLOTTING

If the methods described above are applied to every rectangle in the map, the boundaries and contours will be completely calculated and, at least in principle, ready to be plotted. To avoid inefficient use of the plotter and to assure a smooth appearance, however, it is necessary to sort the line segments.

It is clear that standard algorithms for sorting a list of numbers cannot be used. All of the efficient sorting algorithms (Shell sort [9], quick sort [10], heap sort [11]) make use of the fact that, if two numbers are chosen at random from the list, it is possible to tell which of the two will precede the other when the sort has been completed. With a list of line segments, however, it is usually not possible to tell if two randomly chosen line segments are even part of the same curve.

The simplest approach to this problem would be to compare the position of the last known point on the curve with each endpoint of each line segment in the list. Segments which have been plotted would be

marked in some way to prevent subsequent replotting. Such an approach would work, but it would be very slow if the list were long.

The efficiency of the basic algorithm described above can be improved in two ways: First, we can restrict our definition of a curve, and second, we can exploit the existing order in the list of line segments.

Since we are dealing with a list of line segments, the "curves" which we have been discussing are in fact polygonal paths. Usually, each side of these polygonal paths corresponds to a single line segment. Let us now define a "directed curve" as a polygonal path in which each side points to the right or straight up. Figure 3 shows a curve and its dissection into directed curves.

From the definition of a directed curve, it follows that each of the line segments in a directed curve has a definite starting point and a definite ending point. The x coordinate of the starting point is less than the x coordinate of the ending point, and if these are equal, the y coordinate of the starting point is less than the y coordinate of the ending point. Also, each line segment in a directed curve except the first and the last has a unique predecessor and a unique successor.

The use of directed curves has two practical consequences for the sorting and plotting of a list of line segments. First, as Figure 3 makes clear, complicated curves may be broken up into several directed curves which are plotted separately. This is not desirable, but it has little impact upon the preparation of mechanism maps since it rarely

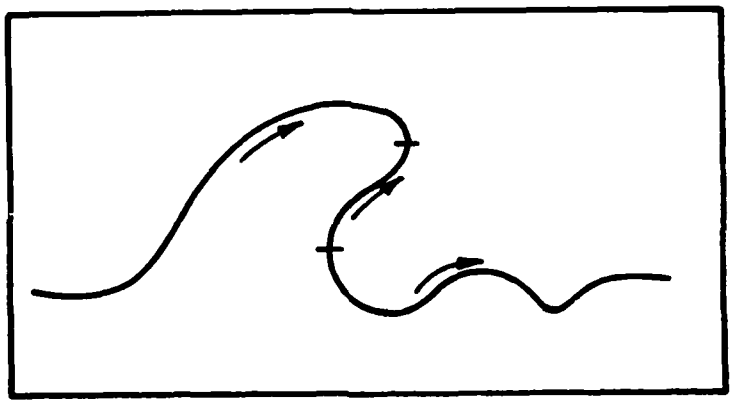

Fig. 3. A Typical Curve and Its Dissection Into Three Directed Curves

occurs. Second, when searching for a successor to the current line segment, the position of the ending point of the current line segment need only be compared to the starting points of the potential successors; the ending points may be ignored. This cuts the length of the search in half.

Let us now investigate how the search time can be cut further by exploiting the existing order in the list of line segments. When we calculate a map, we scan the map in columns of rectangles, working from the left edge of the map to the right edge. Within each column, we scan from the bottom of the column to the top. Within each rectangle, we sort the list of line segments according to the y coordinate of the starting point of the segment. Since the rectangles do not overlap, the ordering of the y coordinate extends throughout the column. The list of line segments is, therefore, highly ordered: it is divided into columns; the segments in one column are ordered from bottom to top; each segment points to the right or straight up.

From this, it is clear that the successor to a given line segment must be either in the current column (the column which contains the current line segment) or in the column just to the right of the current column. Therefore, it is only necessary to search two columns when looking for the successor rather than the whole list. If no successor is found in these two columns, the curve ends.

Further gains in efficiency can be realized by using the fact that the segments are ordered on the y coordinate of their start-

ing points. When searching the current column, the search may start at the current line segment and stop as soon as the y coordinate of a potential successor is so large or so small that segments which are further up or down the column cannot possibly join up with the current segment. A similar strategy may be used in searching the column just to the right of the current column.

5. EXAMPLES

Figure 4 shows two mechanism maps which were calculated and plotted by the methods described here. The same data and constitutive equations were used for both maps, but grids of two different densities were used. It has been claimed [3,8] that a typical map requires the evaluation of deformation rates at 4000 to 6000 points, and maps have been published with at least 6900 evaluation points [12]. By contrast, Figure 4a used evaluations at 441 points, and irregularities in the curves are barely perceptible. Only 169 evaluations were used in the preparation of Figure 4b. The resulting irregularities in the map are visible but hardly objectionable. Clearly, careful use of the data results in a dramatic improvement in efficiency.

ACKNOWLEDGMENT

This work was supported by the Air Force Office of Scientific Research under Contract AFOSR-82-0238.

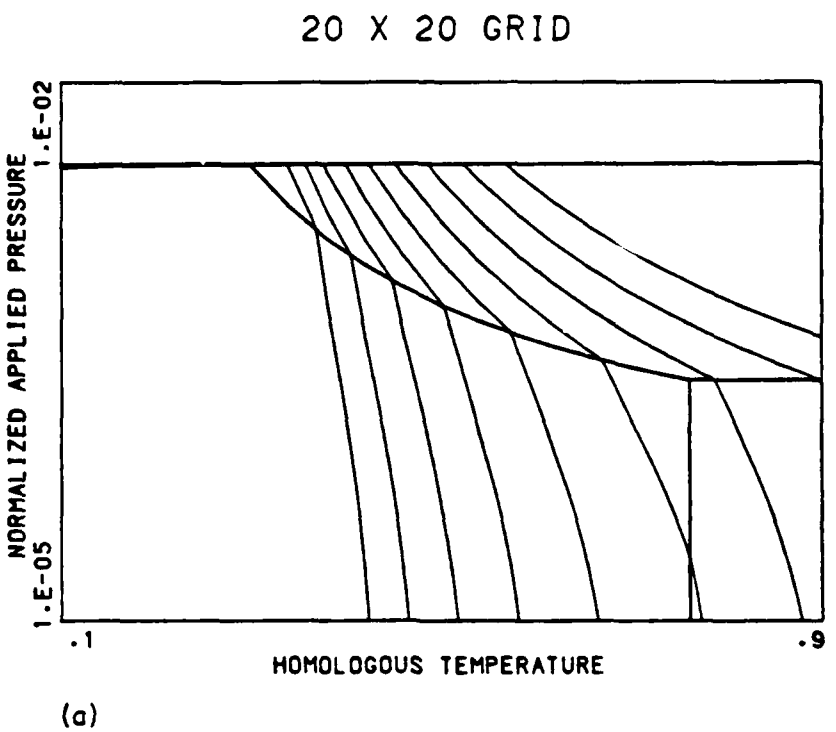

(a)

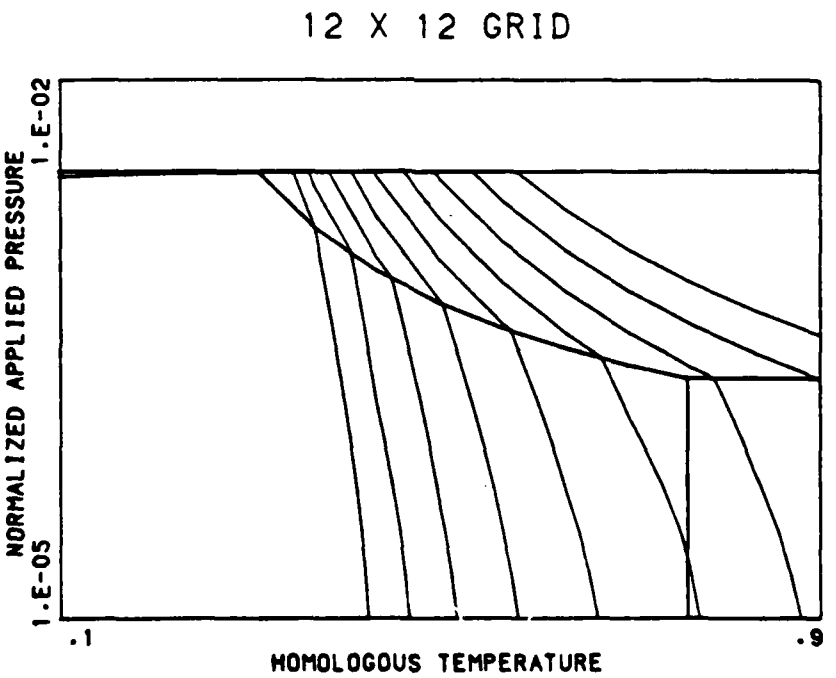

(b)

Fig. 4. Typical Mechanism Maps, Calculated at Two Grid Densities

REFERENCES

1. J. Weertman and J. R. Weertman, in R. W. Cahn (ed.) Physical Metallurgy, North-Holland, Amsterdam, 1965, p. 793.
2. M. F. Ashby, Acta Met. 20 (1972) 887.
3. T. G. Langdon and F. A. Mohamed, Mater. Sci. Eng. 32 (1978) 103.
4. P. A. Urick and M. A. Notis, J. Am. Ceram. Soc. 56 (1973) 570.
5. F. B. Swinkels and M. F. Ashby, Acta Met. 29 (1981) 259.
6. C. Gandhi and M. F. Ashby, Acta Met. 27 (1979) 1565.
7. P. B. Linkson, B. D. Phillips and C. D. Rowles, Corros. Sci. 19 (1979) 613.
8. T. G. Langdon and F. A. Mohamed, J. Mater. Sci. 13 (1978) 1282.
9. D. L. Shell, Comm. ACM 2, No. 7 (1959) 30.
10. C.A.R. Hoare, Comm. ACM 4 (1962) 321.
11. J.W.J. Williams, Comm. ACM 7 (1964) 347.
12. A. Mohan, N. C. Soni and V. K. Moorthy, J. Nucl. Mater. 79 (1979) 312.

AD-A131 514 HOT ISOSTATIC PRESSING OF CERAMIC POWDER COMPACTS(U) 2/2
BATTELLE COLUMBUS LABS OH R R WILLS ET AL. 28 JUN 83
AFOSR-TR-83-0669 AFOSR-82-0238

UNCLASSIFIED F/G 11/2 NL

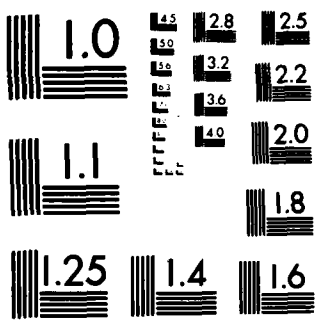

LIST OF CAPTIONS

Fig. 1. Four Possible Topologies for Boundaries in One Rectangle of the Map

a. No boundaries, b. One boundary,

c. Two nonintersecting boundaries,

d. Three intersecting boundaries.

Fig. 2. Treatment of Three Intersecting Boundaries

a,b,c. Location of single boundary if third mechanism were absent. Dotted portion of boundary will be cut off by third mechanism. d. Superposition of a, b, and c. Due to approximations, boundaries do not intersect at a single point. e. Composite map with regions of dominance labeled. Intersection is drawn at centroid of middle triangle in d.

Fig. 3. A Typical Curve and Its Dissection Into Three Directed Curves

Fig. 4. Typical Mechanism Maps, Calculated at Two Grid Densities

END

FILMED

9-83

DTIC